GEORG-AUGUST UNIVERSITÄT GÖTTINGEN

BACHELOR THESIS

Evolution of Droplet Size Distributions in Episodic Precipitation with Time-Dependent Driving

Entwicklung der Tropfengrößenverteilung von rekurrentem Niederschlag mit zeitabhängigem Antrieb

prepared by

Marcel Ernst

from Sulingen

at the Institute for Nonlinear Dynamics

Thesis period: 30th May 2014 to 5th September 2014

First referee: apl. Prof. Dr. Jürgen Vollmer

Second referee: Prof. Dr. Andreas Tilgner

Contents

1 Introduction

1.1 Motivation

The motivation of the present project to advance investigating of the formation of *warm clouds*[1] and their precipitation by an experimental and a numerical approach. The lack of comprehension of the microphysical processes in clouds are key uncertainties in weather and climate prediction [24]. Clouds and precipitation play a key role for the energy budget of the earth [10, pp. 94–95] and about 30% of global rainfall happens in warm clouds (primarily in tropical areas)[24]. Therefore comprehension of the formation and precipitation of those clouds is essential for understanding the consequences of anthropogenic emissions of greenhouse gases on the earth's climate.

On the large scale precipitation arises due to an uprising of a humid air mass in the atmosphere. Due to the pressure drop the air parcel expands and reduces its temperature by adiabatic cooling [19, p. 261].. The decrease of temperature in real atmosphere can be assumed to be linearly with height with about $6 \ldots 7 \frac{\text{K}}{\text{km}}$ [21, p. 45]. Eventually, rise leads to condensation of water droplets when temperature drops below the saturation temperature.

The uprising of wet air parcels is enforced for example by a rising terrain as mountains (*orographic rain*) or due to the clash of a warm and cold air front [18].

Additionally to the net-rising of the air masses I have to consider turbulences and large-scale convective cells within the clouds. The convective cell implicate a periodic up- and downrising of air parcels and thereby an oscillation of temperature on temporal scales of the order of magnitude of the duration of the formation of the clouds and spatial scales of the order of the cloud height. The investigation of convective cells within clouds appears as an essential question for the comprehension of clouds.

The leading question of this thesis is the comprehension of the effect of large-scale convective cells on the evolution of the droplet sizes. How does an occasional increase of temperature in contrast to the ordinary net-decrease effect the droplet size distributions especially regarding shrinkage and evaporation of droplets? How do temperature oscillations change the duration of the droplet growth from nucleation to precipitation? Can I observe phase and frequency locking of those time durations with the characteristic periodic of such oscillations and apply the theory of synchronization here?

In the present thesis I will address these questions using a model system constituting a binary fluid with significant similarities to the system of warm clouds. For better understanding I will now give an overview of the basic ideas and concepts used later in this thesis.

---

[1]Warm clouds are defined by the absence of ice crystals during the formation and precipitation. The droplets stay liquid all the time. [10, pp. 94–95]

Along these lines I go into the demixing in binary fluids, one model for droplet growth and the theory of synchronization.

1.2 Demixing and episodic precipitation in binary fluids

This section is about the dynamics of phase seperation in binary systems and the episodic precipitation occurring when using specific temperature ramps. In figure 2 I show own measurements of episodic precipitation in an exemplary binary fluid using an experimental approach described in section 3. Demixing of binary systems is an universal concept and I can apply it to binary fluids and the system of water and air in clouds.

Figure 1 shows the phase diagram of an generic system in the parameter space of temperature T and composition φ (mass fraction of one of the substances). The phase diagrams visualize the qualitative state in equilibrium for a set of parameters. The blue line represents the coexisting curve or *binodal*. The region below the curve is called miscibility gap where a homogenous mixture of the two substances is not stable and it demixes into two different compositions. In equilibrium the two coexisting phases have the compositions $\varphi_l(T)$ and $\varphi_r(T)$ of the left and the right branch of the binodal at the current temperature T. The single phase region is above the binodal. (see [26])

Within the miscibility gap the green line denotes the *spinodal* between which the diffusion coefficent is negative and demixing unfailingly occurs. Small variabilities of composition will increase between those lines and fast seperation into the two phases occurs. This process is called spinodal decomposition [4] and is shown in the figure (red).

If the state of the system lies between the binodal and the spinodal it is metastable and seperates into two phases of the composition φ_l and φ_r through nucleation of droplets (orange in the figure). Those droplets grow by diffusion of supersaturation and by merging with other droplets due to interfacial energy. Supersaturation is a measure for the imbalance between the current composition and the composition in thermodynamic equilibrium (binodal). (see [26])

In figure 1 the red line represents the path of the system in the phase diagram during episodic precipitation: The decline of temperature is firstly leading to supersaturation which facilitates demixing and therefore induces nucleation of droplets. Those droplets will grow through diffusion and after reaching the critical radius r_b respectively growing beyond the size of Brownian particles they will sediment either upwards or downwards depending on the density differences of the two phases. During the sedimentation the droplets will grow rapidly by coalescence and reduce the droplet number density in the system. After sedimentation which can be denoted as precipitation takes place the composition is on the binodal again and the episodic process can start again. After some time the lighter phase will stay above
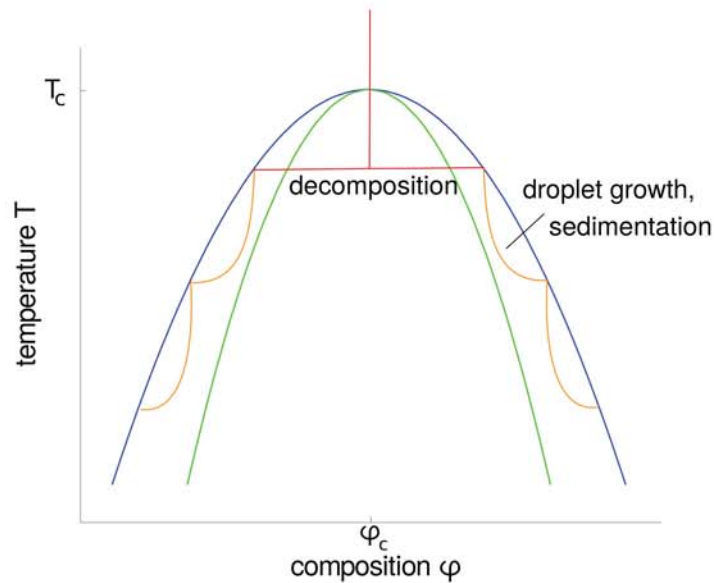
Figure 1: *Sketch of a phase diagram of a generic binary fluid and the path of the composition of the coexisting phases during a temperature ramp if increasing temperature. We see the binodal (blue), the spinodal (green), the fast cooling and spinodal decomposition (red). The outward motion (orange) marks the average composition during the episodic precipitation. (Adapted from [20, p. 19]).*

the other phase and I can observe episodic precipitation in both phases. (see [11, p. 86])

The shown sketch of a phase diagram is generic for binary fluids. Phase diagrams of similar shapes are occurring for example in a binary system of water and air (see figure 3(b)) or in a model system of methanol and hexane which is studied experimentally in [1].

Figure 2 shows the evolution of a precipitation event in an iBE/water system acquired by my own. In the beginning there are only a few droplets from the previous event. After 400 s we observe many small, newly nucleated droplets which are growing and merging within the next 800 s. In the last two images we see that the number of droplets is decreasing rapidly due to coalescence and sedimentation. In the occurring experimental system the droplets never vanish completely but the nucleation of the next droplets starts before.

1.3 Model system and phase diagram

In this section we will consider the experimental system to model warm clouds. As described in [13, 20, 22] a system of iso-butoxyethanol (iBE) and water in a small test-tube is convenient for an experimental approach and shows some similarity to the system of water and air in real warm clouds.

The typical transition temperatures between the homogenous and heterogeneous state of the iBE/water system lie in the temperature range of 25 to 50 °C. This range is convenient

(a) 9400 s

(b) 9800 s

(c) 10 200 s

(d) 10 600 s

(e) 11 000 s

(f) 11 400 s
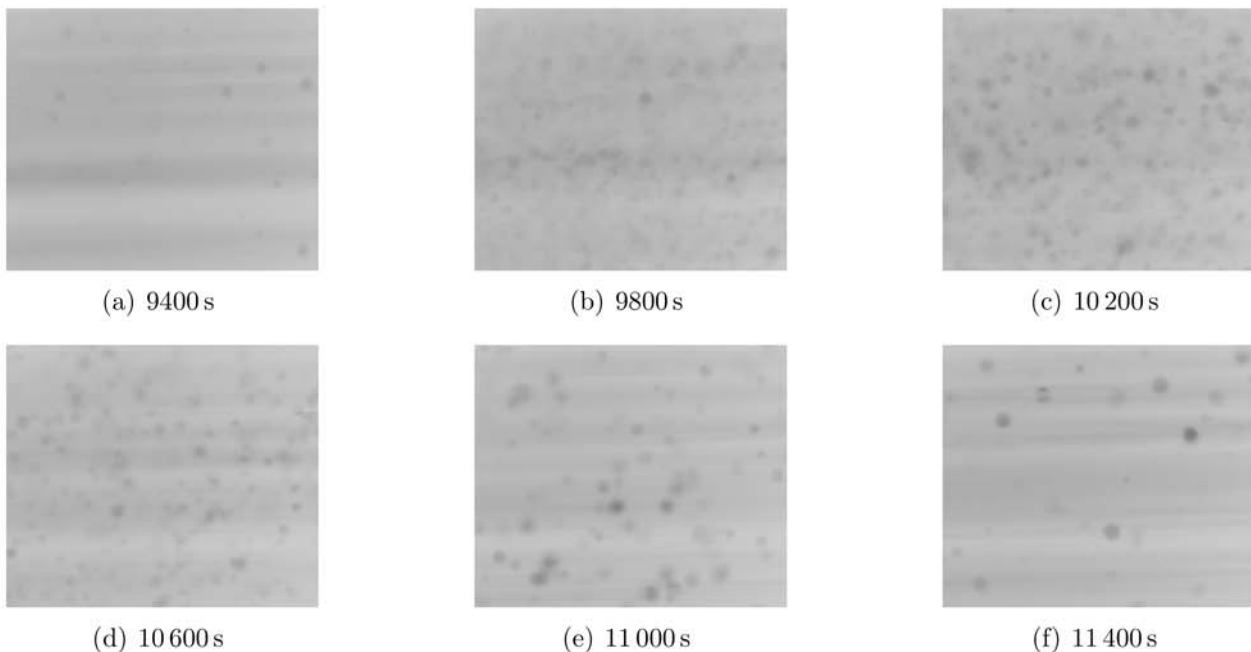
Figure 2: *The images show the evolution of a precipitation event in the binary fluid iBE/water over a time duration of* 2000 s. *They are acquired using the method described in section 3.1 and shown after just inverting them. The used temperature ramp corresponds a constant driving of* $\xi = 2.5 \times 10^{-5} \frac{1}{s}$ *beginning with* $T_0 = 26\,°C$ *(see section 3.1.4).*

for experiments because this is near to room temperature.

Figure 3(a) provides the phase diagram of the considered system. Above the binodal curve the system seperates into two phases with different compositions. The composition of those states in equilibrium are given by the two branches corresponding to a specific temperature in the phase diagram through the lever rule. Below the curve the system is in a homogenous, single-phase mixture. The critical temperature is about $T_c = 25.5\,°C$ [13].

In figure 3(b) we see the air-rich branch of the phase diagram of water and air (e.g. in real clouds) to enable a comparision. After reversing the temperature axis the shapes of both diagrams are looking in principle the same. The demixing occurs here for states in the phase diagram which lie below the curve while by the homogenous state is encountered for the larger temperatures.

This similarity motivates our choice of the model system although we are aware that a similar phase diagram must not lead to the same dynamics. A significant difference of the systems is given by the ratio of the densities of the substances. For a temperature of $T_0 = 25\,°C$ we get [7]:

$$\frac{\varrho_{iBE}}{\varrho_{water}} \approx 0.9 \quad \text{and} \quad \frac{\varrho_{air}}{\varrho_{water}} \approx 1.2 \cdot 10^{-3}. \tag{1}$$
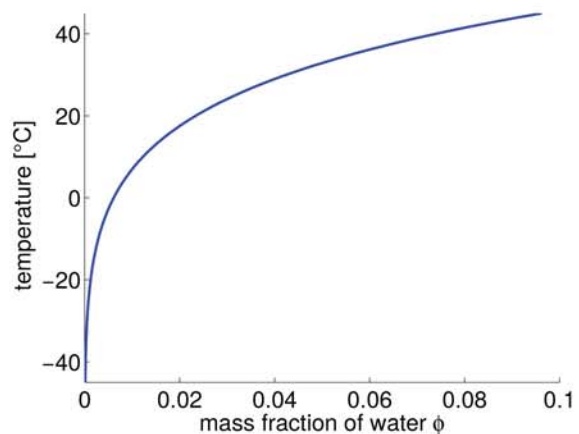
In contrast to the water/iBE system the mass fraction of water in the air-rich branch is much smaller than the fraction of iBE in the water-rich branch.

To examine the qualitative behaviour of such systems the exact phase diagram or occurring temperatures are not important but rather the qualitative shape.

Analogously to clouds — where cooling of the systems leads to demixing — the rising of temperature in the iBE/water system induce phase seperation. We can observe episodic seperation as described in the previous section, too. Because the iBE-rich phase has a lower density there will be an iBE-rich phase above a water-rich phase in a test tube which contains the model system after a transient time. Droplets in the iBE-rich phase in the upper layer are sedimenting downwards, and droplets in the water-rich phase (bottom layer) are rising. The rising droplets are transporting iBE from the bottom to the upper layer. The resulting counterflow mixes water into the sample that enters from the top phase. Altogether this transport leads to a divergence of the average composition of the two phases [11, p. 86].
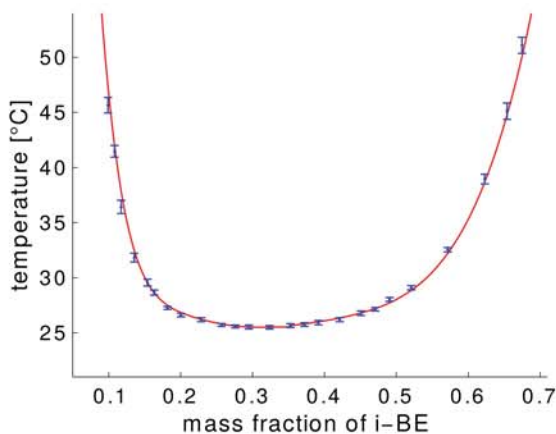
(a) Phase diagram of the model system. (b) Phase diagram of water and air.

Figure 3: *(a) Phase diagram of the investigated iBE/water system. The single-phase region lies below and the biphasic region above the curve. (Adapted from [13]) (b) Air-rich phase of the phase diagram of a water/air system (e.g. in warm clouds). The single-phase region lies above and the biphasic region below the curve. The diagram is created by Martin Rohloff using the formula for the saturated vapor pressure of water in air from [3]. To get the mass fraction the partial pressure of air has to be considered wherefore we use the approximation of $p_{air} \approx 1 \times 10^5 \, \mathrm{Pa}$.*

1.4 Model for droplet growth

In this section I describe a model and a differential equation for droplet growth with a constant and positive external driving and a constant droplet number density. In this sense I consider a system with an increasing amount of saturation. The radius growth described in

the differential equation refers to the radius of the characteristic size of the largest droplets within the system. The approach is adapted from Tobias Lapp [12].

Beginning with nucleated droplets and a supersaturated system the supersaturation is decreased by diffusion towards the droplets. After a while the droplets reach a critical radius and start to sediment. This leads to coalescence where the sedimenting droplets collect smaller droplets due to the indifferent sedimentation velocities. This process entails rapid growth of the larger droplets and a fast decrease of the number of droplets.

In figure 4(a) I show the growth rate of the characteristic droplets in dependence of their radius. Both values are normalized using the bottleneck radius r_b where minimal growth rate occurs (See section 2.1.1 on that account). For either small and large droplets the dominant effects are illustrated.

Droplets whose radius is smaller than the bottleneck radius are mainly growing by diffusion of supersaturation in their neighborhood. The diffusional volume growth $\dot{V}$ occurs to be independent of the droplet radius r and is given by

$$\dot{V} = 4\pi r^2 \dot{r} = \frac{\xi}{n} \tag{2}$$

where $\xi(t)$ describes the time-dependent increase of the droplet volume fraction within the observed phase and n the constant droplet number density. This entails that $\dot{r} \propto r^{-2}$. Consequently diffusive growth is a fast process for small radii.

It becomes negligible for radii above the bottleneck radius with respect to the dominating coalescence. The sedimenting droplets will undergo a velocity

$$u_{\text{sed}} = -\kappa r^2 \tag{3}$$

due to Stoke's buoyancy formula whereby κ represents a pre-factor [2, p. 234]. The constant κ is given by the relation [2, p. 234]

$$\kappa = \frac{2\,\Delta\varrho\,g}{9\mu} \tag{4}$$

where g is the gravitational acceleration, $\Delta\varrho$ the difference of the mass densities of the two states and μ the corresponding viscosity.[2]

At that velocity a droplet crosses a volume of $dV_{\text{cross}} = |u_{\text{sed}}|\,\pi r^2 dt = \kappa r^2 \pi r^2 dt$ per unit time with the cross section πr^2 of the droplet.

In case it is the first sedimenting through this volume the droplet volume fraction $\Phi(t)$ for

---

[2]To determine $\kappa(T)$ using equation (4) I need the densities of the two occurring phases and the viscosity. The temperature dependence of those values is given in the appendix.

the time t and starting time t_0 is

$$\Phi_{t_0}(t) = \int_{t_0}^{t} \xi(t') \mathrm{d}t' \tag{5}$$

because $\xi(t)$ denotes the change of droplet volume fraction. Using the collection efficency ϵ which describes the fraction of gathered droplets in the volume which is crossed per unit time I get

$$\dot{V}(t) = 4\pi r^2 \dot{r} = \epsilon \kappa r^2 \pi r^2 \Phi_{t_0}(t). \tag{6}$$

Hence $\dot{r} \propto r^2$ which is irrelevant for small r, and dominant for $r \gtrsim r_b$.

Combining those two terms the following equation shows the relation between the growth rate of the droplet radius [11, p. 113]:

$$\dot{r}(t) = \frac{\xi(t)}{4\pi n} \frac{1}{r^2} + \frac{\epsilon \kappa}{4} r^2 \Phi_{t_0}(t). \tag{7}$$

## 1.5 Theory of synchronization

Convective cells in clouds lead to an oscillation of temperature and thereby to a time-dependent driving $\xi(t)$ which is assumed here to be periodic. The fact that even a constant driving $\xi(t) = \xi_0 = \mathrm{const}$ results in episodic precipitation with a frequency ω_0 of section 1.2 leads to my interest in synchronization: I consider episodic precipitation with constant driving ξ as a forced nonlinear oscillator with frequency ω_0, and explore the episodic precipitation affected by an periodic driving, $\xi(t) = \xi_0 (1 + A \cos(\omega t))$ with amplitude A and frequency ω. As background to this I study I will describe some basic concepts and notations [15, pp. 44–66].

For an amplitude $A = 0$ the precipitation has a frequency of ω_0 whereby the difference in frequency of the external forcing and the oscillator $\omega - \omega_0$ is called detuning. A weak additional force with amplitude $A \leq 1$ will not change the amplitude of the episodic precipitation. However it may change the phase and the frequency. For a positive amplitude $A > 0$ we get a phase shift φ and a frequency shift to Ω whereby in general $\Omega \neq \omega_0$.

For $\omega = \omega_0$ one observes phase locking towards a specific phase φ_s between the driving and response. Establishing such a phase locking requires longer time for smaller amplitudes. In case of small detuning ($|\omega_0 - \omega| \leq \omega_0$) we still observe frequency locking $\Omega = \omega_0$ for large enough amplitudes, and thereby phase locking to a phase $\varphi = \varphi_s + \Delta\varphi$.

This results in regions in the parameter space $[A, \omega]$ where we observe synchronization. Those regions are called *Arnold tongues* (see the $1 : 1$ region in figure 4(b)). Larger amplitudes of external forcing results in broader Arnold tongues.

In addition to frequency locking with $\Omega = \omega_0$ we also observe Arnold tongues for arbitrary ratios of frequencies $m\Omega = n\omega$ with $m,n \in \mathbb{N}$ of figure 4(b). In practice only ratios with small numbers are accessible for experiment. For example the case $m = 2$ and $n = 1$ amount to the case $2\Omega = \omega$ there the episodic precipitation arises every second period of the driving $\xi(t)$. In general Arnold tongues with larger m,n are smaller which associates to larger necessary amplitudes to reach synchronization.
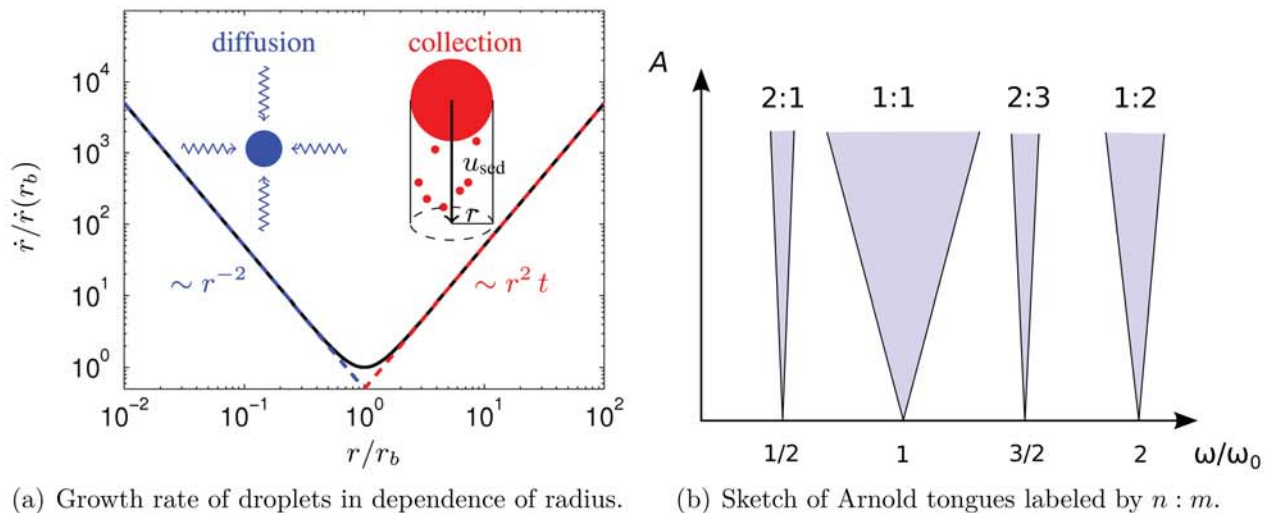
(a) Growth rate of droplets in dependence of radius.   (b) Sketch of Arnold tongues labeled by $n : m$.

Figure 4: *(a) Sketch of the growth rate $\dot{r}$ of the radius of large droplets in dependence of the radius and a sketch of the dominant effects. The radius is normalized using the bottleneck radius r_b where minimal growth occurs (adapted from [12]). (b) Sketch of generic Arnold tongues for driving frequency $\frac{\omega}{\omega_0} = \frac{m}{n}$ and amplitude A (reproduced from [15]).*

1.6 Outline

This thesis is divided into two main parts. First I will present a numerical approach to analyze the synchronization for a periodic driving with small amplitudes in chapter 2. This work revisits results of Julian Vogel [22] who found first experimental evidence for synchronization of episodic precipitation. Beginning with the model described in section 1.4 I will compute and examine the corresponding Arnold tongues. In the second part I will analyze the effect of larger amplitudes on the evolution of the droplet size distribution using an experimental approach and a specific model system given by a binary fluid of iso-butoxyethanol (iBE) and water. I will describe the experimental setup and the methods of image processing and droplet detection in chapter 3. This work builds on methods established by Martin Rohloff and Tobias Lapp (see [20] and [11]). Considering their experiments with positive constant driving I will investigate the evolution of the size distributions especially for shrink-

ing droplets due to negative driving (chapter 3.2). My main results will be discussed in the conclusions, chapter 4.

2 Synchronization in episodic precipitation with time-dependent driving

This chapter treats the impacts of small amplitudes in periodic driving on the growth of droplets in warm clouds. I will apply the concept and framework established in section 1.4 and 1.5. More specifically I will examine the effect of an external, periodic driving on the growth time which is the time duration between nucleation and the precipitation while reaching the maximal radius. Small amplitudes mean in the context of this chapter that the driving $\xi(t)$ of the systems remains positive. This corresponds to monotonic change of temperature in a real system. In that case the model described in section 1.4 can be applied.

2.1 Numerical analysis of synchronization

I will use a numerical approach to investigate the change of growth time and examine synchronization due to a periodic driving of the system. Rather than specifying our system in detail I will take the perspective of a generic, nondimensionalized model that will be dervied in section 2.1.1.

The periodic driving will be an alternation between two constant, positive values ξ_{max} and ξ_{min} of driving $\xi(t)$. In figure 5 I show a sketch of this driving type and introduce variables characterizing its amplitude and period. For comparision, I also examine sinusoidal driving $\xi(t)$.
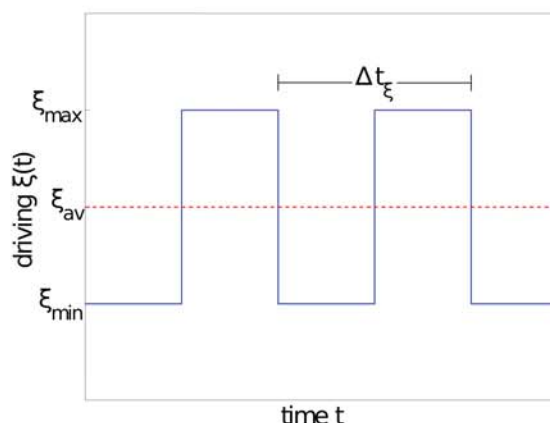
Figure 5: *Sketch of square-wave driving to illustrate the used variables.*

First we address the question under which conditions there is synchronization of the growth time Δt with the periodicity Δt of $\xi(t)$ and examine the shape of the occurring Arnold tongues.

2.1.1 Nondimensional model for droplet growth

For convenience of the numerical integration of a generic system I rephrase and nondimensionalize equation (7):

The first term in this equation is proportional to r^{-2}. It is not suitable for numerical integration due to the singularity at $r = 0$. Instead of looking at the droplet radii I therefore consider the volume $v \propto r^3$, which leads to a constant first with no singularity:

$$\frac{\mathrm{d}r^3}{\mathrm{d}t}(t) = \frac{3\xi(t)}{4\pi n} + \frac{3\epsilon\kappa\Phi_{t_0}(t)}{4}r^4,$$

$$\dot{\Phi}_{t_0}(t) = \xi(t) \tag{8}$$

The first term corresponds to the diffusional growth and the second term to the growth by coalescence. The diffusion dominates for small radii $r \lesssim r_b = [\pi n\epsilon\kappa t]^{1/4}$ and coalescence for larger radii $r \gtrsim r_b$ such that $\dot{r}$ is minimal at the bottleneck radius r_b. Note that the radius r_b fulfills the equation

$$\left.\frac{\mathrm{d}\dot{r}}{\mathrm{d}r}\right|_{r=r_b} = 0. \tag{9}$$

For non-dimensionalization I use the bottleneck time and radius of the corresponding system with $A = 0$. Because the growth by coalescence is negligible for times t smaller than the bottleneck time t_b I integrate the first term of (8) to the bottleneck radius r_b for constant driving $\xi(t) = \xi_0$ (amplitude $A = 0$) and get

$$r_b^3 = \int_0^{r_b^3} \mathrm{d}r_b^3 = \int_0^{t_b} \frac{3\xi_0}{4\pi n_0}\mathrm{d}t = \frac{3\xi_0 t_b}{4\pi n_0} \tag{10}$$

with the occurring droplet number density n_0. Using $r_b = [\pi n\epsilon\kappa t]^{1/4}$ I obtain

$$t_b = \left(\pi\frac{4^4}{3^4}\frac{n_0}{(\epsilon\kappa)^3\xi_0^4}\right)^{1/7}, \tag{11}$$

$$r_b = \left(\frac{3}{4\pi^2}\frac{\xi_0}{\epsilon\kappa n_0^2}\right)^{1/7} \tag{12}$$

In terms of the resulting nondimensional coordinates

$$\tilde{n} := \frac{n}{n_0}, \quad v := \frac{r^3\,\tilde{n}^{6/7}}{r_b^3}, \quad \tau := \frac{t}{t_b\,\tilde{n}^{1/7}}, \quad \tilde{\xi}(\tau) := \frac{\xi(t)}{\xi_0} \quad \text{and} \quad \tilde{\Phi}_{\tau_0}(\tau) = \frac{\tilde{n}^{1/7}}{\xi_0\,t_b} \tag{13}$$

14

and assuming $\frac{\mathrm{d}\tilde{n}}{\mathrm{d}\tau} = 0$, I rephrase equation (8) as

$$\frac{\mathrm{d}v}{\mathrm{d}\tau} = \tilde{\xi}(\tau) \cdot \underbrace{\frac{3\xi_0}{4\pi}\frac{t_b}{r_b^3}}_{1} + \tilde{\Phi}_{\tau 0}(\tau) v^{4/3} \cdot \underbrace{\frac{3\epsilon\kappa\xi_0}{4}r_b t_b^2}_{1}$$

$$\Leftrightarrow \frac{\mathrm{d}v}{\mathrm{d}\tau} = \tilde{\xi}(\tau) + \tilde{\Phi}_{\tau 0}(\tau)\, v^{4/3}. \tag{14}$$

To show that the choice of $n = $ const is justified I introduce k which is defined as the ratio of the average radius $\langle R \rangle$ and the critical radius R_c that seperate growing from shrinking droplets in an ensembly of droplets performing competitive growth by diffusion. According to Clark et al.[5] and Vollmer et al. [23] the ratio is given by

$$k = \frac{\langle R \rangle}{R_c} = 1 + \frac{\xi}{4\pi\sigma Dn},$$

where the Kelvin length *sigma* and diffusion coefficient D. Only in the regime of small values of k there is noticeable evaporation of droplets [23] and thereby a decrease of the droplet number density n. For any $k \gtrsim 5$ there is no evaporation of droplets [23].

In episodic precipitation studies k takes values of about $10^4 \ldots 10^6 \gg 1$ in the considered iBE/water system [23] and $k \gtrsim 5$ in clouds [23]. For these values there is no noticeable droplet evaporation, such that $n\tilde{=}$const. Hence, I expect that the results in this chapter are not restricted to specific binary systems. Rather they apply to broad classes of binary systems whose droplet growth obeys the theory outlined in section 1.4.

In case of square-wave $\xi(t)$ shown in figure 5 the relative amplitude A is defined as

$$A = \frac{\xi_{max} - \xi_{av}}{\xi_{av}}. \tag{15}$$

Because I am analyzing synchronization due to oscillation I look at the ratio of the growth time $\Delta t(\xi_{av})$ for constant driving ξ_{av} and the period Δt_ξ of $\xi(t)$. Thus I define the value

$$p = \frac{\Delta t(\xi_{av})}{\Delta t_\xi} = \frac{\omega}{\omega_0} \tag{16}$$

as control parameter of my measurements (of figure 4(b)). Here $\Delta t(\xi_{av}) \propto \omega_0^{-1}$ characterizes the frequency of the unpertubated episodic precipitation arising for constant $\xi(t) = \xi_{av}$, and $\Delta t_\xi \propto \omega^{-1}$ characterizes the frequency of the pertubation (of figure 5). For example in case of $p = 2$ we have a full period of precipitation (growth time) in two periods of $\xi(t)$.

Former studies show that for $\xi(t) = \xi_{av}$ the period is $\Delta t(\xi_{av}) \approx 2.44 t_b$ with the bottleneck

time defined in section 2.1.1 [12]. Using equation (16) leads to the relation

$$\Delta\tau_\xi = \frac{\Delta t_\xi}{t_b} = \frac{\Delta t(\xi_{av})}{t_b \, p} = \frac{2.44}{p} \tag{17}$$

which is used for the aim of the numerical integration.

2.1.2 Growth time of droplets

In this section I describe the methods to calculate the dependence of the growth time for given p and A from the initial phase in the periodic driving $\tilde{\xi}(\tau)$. Starting from equation (14) I numerically compute the growth time $\Delta\tau$ using the described dimensionless variables.

In case of the square-wave the function $\tilde{\xi}(\tau)$ is given by

$$\tilde{\xi}(\tau) = \begin{cases} 1 - A, & \text{for } \frac{\tau}{\Delta\tau_\xi} \in [0,0.5] + \mathbb{Z} \\ 1 + A, & \text{for } \frac{\tau}{\Delta\tau_\xi} \in [0.5,1] + \mathbb{Z} \end{cases} \tag{18}$$

and for sinusoidally shaped $\xi(t)$ I use

$$\tilde{\xi}(\tau) = 1 - A \sin\left(\frac{2\pi\tau}{\Delta\tau_\xi}\right). \tag{19}$$

Starting from the initial phase $\tau_0 \in [0,\Delta\tau_\xi]$ I integrate equation (14) in order to determine the time τ_1 where the droplet volume diverges. In order to show that the growth time $\Delta\tau = \tau_1 - \tau_0$ is alway finite I use the differential equation (14) for larger volumes v where the first term $\tilde{\xi}$ may be neglected. Seperation of variables gives:

$$\int_{\tau_0}^{\tau_1} \tilde{\xi}_{\min}\tau d\tau < \int_{\tau_0}^{\tau_1} \tilde{\Phi}_{\tau_0}(\tau)d\tau = \int_{v_0}^{\infty} \frac{dv}{v^{4/3}},$$
$$\tilde{\xi}_{\min}\frac{\tau_1^2 - \tau_0^2}{2} < \left[-3v^{-1/3}\right]_{v_0}^{\infty} = \frac{3}{v_0^{1/3}} < \infty, \tag{20}$$

such that τ_1 is finite in case of positive minimal driving $\tilde{\xi}_{\min} > 0$.

The algorithm for the numerical integration starts with setting of the parameters p, A and $\frac{\tau_0}{\Delta\tau_\xi} \in [0,1]$. Beginning with $v = 0$ and $\tau = \tau_0$ I numerically integrate the volume until v exceeds the threshold v_{max} to estimate the divergence time τ_1. The threshold is set to $v_{max} = 10^{10}$ and is large enough that a larger volume of v_{max} has no significant effects on τ_1. To integrate equation (14) I determine $\tilde{\Phi}_{\tau_0}(\tau)$ by analytically integrating $\int_{\tau_0}^{\tau} \tilde{\xi}(\tau')d\tau'$. For

the sinusoidal driving (19) this yields,

$$\int_{\tau_0}^{\tau} \tilde{\xi}(\tau')\mathrm{d}\tau' = \left[\tau' - \frac{A\Delta\tau_\xi}{2\pi}\cos\left(\frac{2\pi\tau'}{\Delta\tau_\xi}\right)\right]_{\tau_0}^{\tau} \tag{21}$$

and using if-conditions I implement it for square-wave driving, too.

For the numerical implementation of equation (14) I use the classical fourth-order Runge-Kutta method [9, p. 138] with a time step of $\Delta = 10^{-4}\ldots 10^{-3}$.

In figure 6(a) we exemplary see the dependence of the volume v from time τ and the used square-wave $\tilde{\xi}(\tau)$ with the parameters $p = 2$, $A = 0.5$ and $\frac{\tau_0}{\Delta\tau_\xi} = 0.2$. Because of the wide range of volumes occurring I use a logarithmic representation where the slope corresponds to the relative growth rate:

$$\frac{\mathrm{d}\log v}{\mathrm{d}\tau} \propto \frac{1}{v}\frac{\mathrm{d}v}{\mathrm{d}\tau} \propto \frac{1}{r^3}r^2\dot{r} = \frac{\dot{r}}{r}. \tag{22}$$

We see the three phases of droplet growth: In the first part the relative growth is large because of the constant volume growth. This effect is decreasing in the region of the bottleneck. After some time the coalescence term dominates and leads to a rapid increase in relative growth until the divergence of radius at the finite time τ_1.

The volume is increasing slowly in the beginning because the second term in the equation is still negligible and for larger times the growth rises rapidly. At the first jump of $\tilde{\xi}$ we observe an change of the slope of the volume because of a changed prefactor of diffusional growth in the beginning.
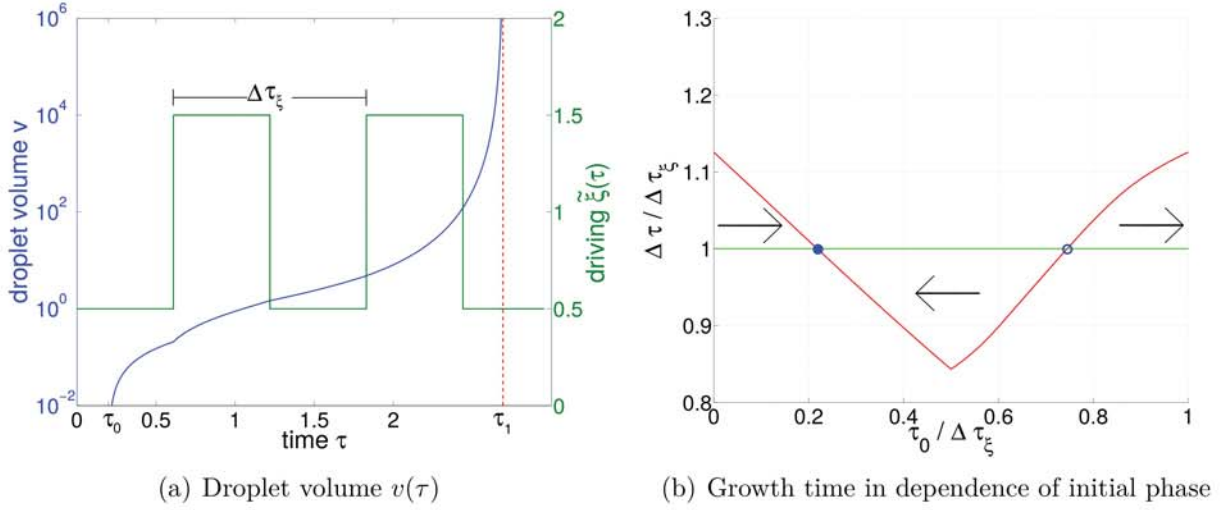
Figure 6(b) shows the dependence of the growth time $\Delta\tau = \tau_1 - \tau_0$ from the intital phase τ_0 for a square-wave $\tilde{\xi}(\tau)$ and parameters $p = 1$ and $A = 0.5$. Varying the initial phase between 0 and 1 leads to changes of the growth time of about $15\,\%$ relative to the value for $\tilde{\xi}(\tau) = 1$. The plotted times are normalized by the period of the driving $\tilde{\xi}(\tau)$ such that they reflect the phase of the periodicity of the signal. When $\frac{\Delta\tau}{\Delta\tau_\xi} > 1$ the phase increases, and it decreases otherwise. Consequently we obtain pairs of stable and unstable fixed[3] points whenever $\frac{\Delta\tau}{\Delta\tau_\xi}$ intersects 1.

2.1.3 Synchronization

A convenient graphical way to follow the dynamics are phase maps showing the phase $\frac{\tau_1}{\Delta\tau_\xi}$ mod $1 \in [0,1]$ after precipitation in dependence of the initial phase $\frac{\tau_0}{\Delta\tau_\xi} \in [0,1]$. A few examples are shown in figures 7(a) to 7(c).

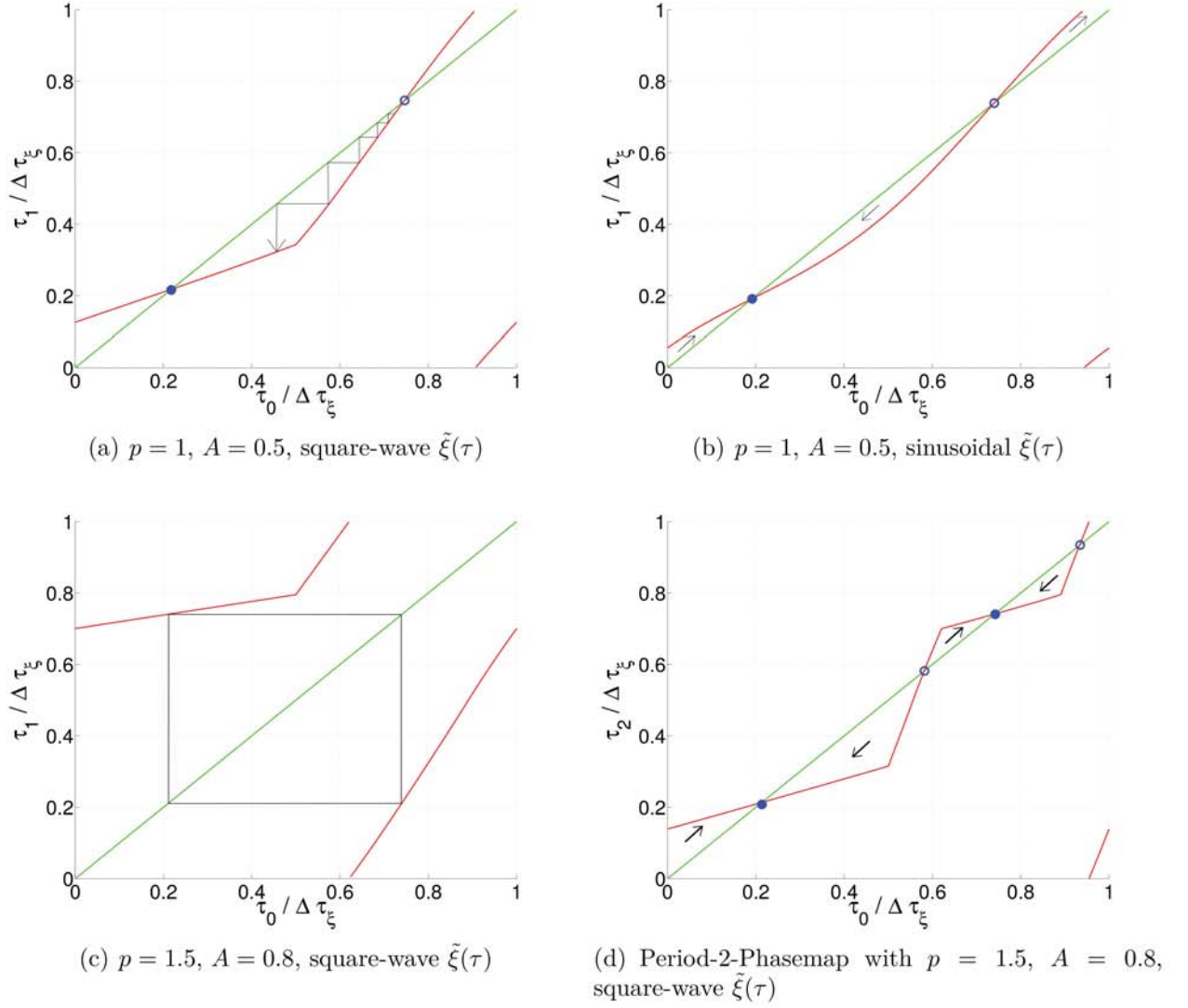In figure 7(a) we see the phase map corresponding to the plot in figure 6(b). The common

---

[3]Slightly differing phases are attracted by a stable and repelled by unstable fixed points.

(a) Droplet volume $v(\tau)$

(b) Growth time in dependence of initial phase

Figure 6: *In these figures I use a square-wave $\tilde{\xi}(\tau)$ with $A = 0.5$ and (a) $p = 2$ and (b) $p = 1$, respectively. (a) Droplet volume v and driving $\tilde{\xi}$ for initial time $\tau_0 = 0.2\Delta\tau_\xi$. The red, dashed line shows the divergence time τ_1. (b) Growth time $\Delta\tau = \tau_1 - \tau_0$ in dependence of initial phase $\frac{\tau_0}{\Delta\tau_\xi}$ (red). The green line is a reference curve for $1:1$ locking where $\Delta\tau = \Delta\tau_\xi$. The filled circles denotes the stable and the unfilled circles the unstable fixed points and the arrows the direction of the change of phase.*

cob-webbing construction [6] nicely shows the approach of the system to the phase-locked state where $\frac{\tau}{\Delta\tau_\xi} = 0.21 = const$. A sufficient criterion for the stability of a fixed point in phase maps $M : [0,1] \to [0,1]$ is given by the absolute value of the derivative of the map $\left|M'(\frac{\tau_0}{\Delta\tau_\xi})\right| < 1$ [6, p. 25] at a fixed point τ_* where $M(\frac{\tau_*}{\Delta\tau}) = \frac{\tau_*}{\Delta\tau}$. Applied to the phase maps in figure 7 this requires a crossing of the identity (green line) with an absolute slope smaller than one. Hence, the fixed point at $\frac{\tau_s}{\Delta\tau} = 0.21$, is stable and the other one, $\frac{\tau_u}{\Delta\tau} = 0.75$, is unstable. This leads to synchronization of the periods regarding the fixed point τ_s. Analogous behaviour is observed in the phase map for a sinusoidal shape of the driving (figure 7(b)). Naturally, the shape of the maps are relatively similar, and hence also the positions of the fixed points do not differ much.

To analyze the existence of stable fixed points numerically we calculate τ_1 for N_0 uniformly distributed values of $\frac{\tau_0}{\Delta\tau_\xi} \in [0,1]$. Within the implementation we do not use phase maps for this analysis but the divergence time $\tau_1(\tau_0)$ to avoid the jumps occurring in the maps. Now we check whether there is a phase τ_0 so that for the previous computed value the growth time $\frac{\tau_1}{\Delta\tau_\xi}$ is above $p + \frac{\tau}{\Delta\tau_\xi}$ and for the subsequent value below for one $p \in \mathbb{Z}$. This corresponds $\frac{\tau_1}{\Delta\tau_\xi}$ mod 1 is crossing the identity and $\frac{\Delta\tau}{\Delta\tau_\xi}$ crossing an integer from above. Besides that we evaluate whether the condition for the slope is fulfilled, too.

18

(a) $p = 1$, $A = 0.5$, square-wave $\tilde{\xi}(\tau)$

(b) $p = 1$, $A = 0.5$, sinusoidal $\tilde{\xi}(\tau)$

(c) $p = 1.5$, $A = 0.8$, square-wave $\tilde{\xi}(\tau)$

(d) Period-2-Phasemap with $p = 1.5$, $A = 0.8$, square-wave $\tilde{\xi}(\tau)$

Figure 7: *Dependence of divergence time $\frac{\tau_i}{\Delta\tau_\xi}$ mod 1 after $i = 1$ or 2 cycles starting from $\frac{\tau_0}{\Delta\tau_\xi}$ (phase map) for different parameters p and A and different shapes of $\tilde{\xi}(\tau)$. For this plot the integration is done for 250 uniformly distributed phases τ_0 with $\Delta = 10^{-4}$. The filled circles denote stable and open circles unstable fixed points. In figure (c) I show the stable period-2-cycle.*

Due to the fact that after precipitation of the droplets a new period is beginning we use the divergence time τ_1 as the new initial phase and τ_2 as new divergence time and so on. This allows phase-cycles of larger period, e.g. we have a period-2-cycle if $\tau_2 \equiv \tau_0 \mod \Delta\tau_\xi$.

Starting from the computed values of $\tau_1(\tau_0)$ we calculate τ_m for $m > 1$. Using the computed values of τ_{m-1} we plug in $\frac{\tau_{m-1}}{\Delta\tau_\xi} \mod 1$ in $\tau_1(\tau_0)$ due to periodicity of the driving and calculate the next value. If the required value is not one of the N_0 computed values the linearization between the computed values are used as an approximation. Because the function $\tau_1(\tau_0)$ is steady in all relevant cases this is justified.

In figure 7(c) we see the phase map for $p = 1.5$ and $A = 0.5$. It has no fixed points, and thereby no period-1-cycle. To look for a period-2-cycle we plot $\frac{\tau_2}{\Delta\tau_\xi} \mod 1$ in dependence of $\frac{\tau_0}{\Delta\tau_\xi} \mod 1$ (figure 7(d)). This map has two stable fixed points at about $\frac{\tau_0}{\Delta\tau_\xi} = 0.2$ and 0.67. During the corresponding period-2-cycle the phase at the time of precipitation/nucleation is alternating between those two values. This means that the same phase is achieved in every second precipitation cycle. Numerically the stability of the fixed points in period-m-cycles is examined as above after calculating τ_m.

2.2 Examination of the Arnold tongues

In this section I show the Arnold tongues for the synchronization of phases. To examine those tongues I compute the sections in the parameter space of p and A for which we observe a period-m-cycle. I also study the phase of the stable fixed point in the $1 : m$ Arnold tongues for $m = 1 \cdots 8$.

2.2.1 Calculation of Arnold tongues

For the numerical calculation of the Arnold tongues I analyze the existence of periode-m-cycles as described in the previous section for a huge set of parameters p and A. To reduce computation time I integrate $\tau_1(\tau_0)$ for $N_0 = 100$ values with an accuracy of $\Delta = 10^{-3}$. I calculate the fixed point in period-1-cycles more precisely to enable better analysis of the results. To achieve this I calculate $\tau_1(\tau_0)$ for 40 values in the neighborhood (± 0.02) of the calculated stable fixed point with an accuracy of $\Delta = 10^{-4}$.

Besides the Arnold tongues for a square-wave driving I also calculate the tongues for sinusoidal shape to examine the impact of the shape of the periodic function $\xi(\tau)$ on the phase locking.

2.2.2 Arnold tongues in parameter space

Figure 8 shows the computed Arnold tongues for the parameter space for 100 values of the amplitude $A \in [0, 0.99]$ and in all 4000 values of $p \in [0, 2]$ and $p \in [7, 9]$. The different colors mark Arnold tongues corresponding to period-n-cycles for $n \in [1, 2, 3]$ for sinusoidal (bottom) and square-wave driving (top). respectively. I show the neighborhood of the first period-1 Arnold tongue, and exemplary of the eighth tongue to visualize the difference.

There are Arnold tongues of period-1 near p-values which are integer and period-n Arnold tongues near values with $p = m/n$. The tongues are broadening from smaller to larger amplitudes beginning with a width of 0 for the amplitude $A = 0$. After all, in case of constant driving ($A = 0$) the growth time is $\Delta\tau(\tilde{\xi}_0) = 2.44$, and according to equation (17) this corresponds to p periods of the driving ($\Delta\tau_\xi$).

The width of the tongues of higher order is smaller, and likewise they are smaller for sinusoidal as compared to square-wave driving. The gaps within the period-3 Arnold tongues are probably numerical artefacts arising when the width of the tongue is smaller than the distance of the computed points in parameter space.

Figure 9 shows the phasemap as introduced earlier for a few succeding values of p (left) and A (right) whereby the other value is kept constant. For fixed $A = 0.5$ the curve in the phasemap (figure 9(a)) has a similar shape for all p, but is displaced parallel in the vertical direction with nearly constant distances for constant increments of p. There is occurring an abrupt increase of the slope at $\tau_0 \equiv 0.5(\mod \Delta\tau_\xi)$ for all curves. $\frac{\mathrm{d}\tau_1(\tau_0)}{\mathrm{d}\tau_0} < 1$ for $\frac{\tau_0}{\Delta\tau_\xi} \in [0, 0.5]$ and > 1 otherwise.
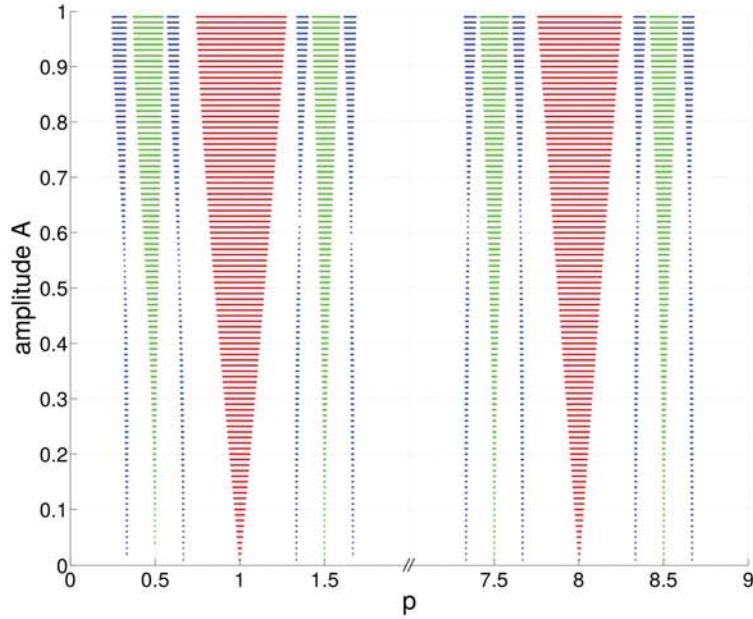
Using equation (17) I know for the growth time in case of constant $\tilde{\xi}(\tau) = 1$ that it fulfills $\Delta\tau = p\Delta\tau_\xi$. This leads to $\tau_1 = \tau_0 + p\Delta\tau_\xi$, thus explaining the p-dependent shift of the curves.

For fixed $p = 0.9$ and increasing amplitudes the smaller slope is decreasing and the larger slope is increasing further. In the following I will argue why this behaviour is plausible:
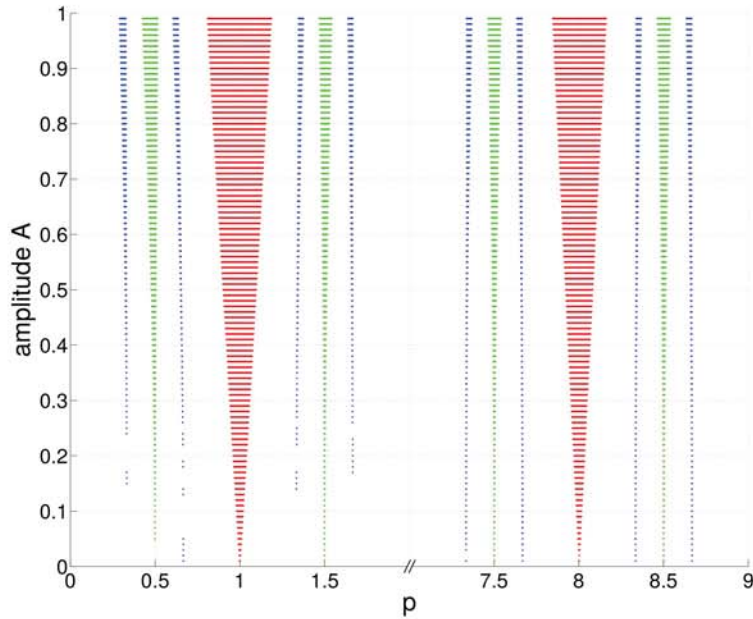
We know that $\tilde{\Phi}_{\tau_0}(\tau) = \int_0^\tau \tilde{\xi}(\tau)\mathrm{d}\tau$ due to equation (5). I assume $\tilde{\xi}(\tau) = 1 + A\zeta(\tau)$ whereby specific choices of $\zeta(\tau)$ lead to square-wave (18) and sinusoidal (19) driving. Using equation (5) I integrate equation (14) beginning from the bottleneck time and neglecting the diffusional growth,

$$\Gamma := \int_{v_b=1}^\infty v^{-4/3}\mathrm{d}v = 3 \;\; = \;\; \int_{\tau_b=1}^{\tau_1} \tilde{\tilde{\Phi}}_{\tau_0}(\tau)\mathrm{d}\tau$$

$$= \int_1^{\tau_1} \tilde{\Phi}_0(\tau) - \tilde{\Phi}_0(\tau_0)\mathrm{d}\tau$$

$$= \int_1^{\tau_1} \tilde{\Phi}_0(\tau)\mathrm{d}\tau - (\tau_1 - 1)\,\tilde{\Phi}_0(\tau_0) \quad\quad (23)$$

(a) Arnold tongues for square-wave driving

(b) Arnold tongues for sinusoidal driving

Figure 8: *Arnold tongues for amplitude $A \in [0,1]$ and $p \in [0,2] \cup [7,9]$ for uniformly distributed values in the parameter space. The dots corresponds to stable period-n-cycles, i.e. to Arnold tongues of period-n-cycles with $n = 1$ (red dots), $n = 2$ (green dots) and $n = 3$ (blue dots), respectively. Accordingly the tongues for $p \in [0,2]$ corresponds to $4:1$, $4:2 = 2:1$, $4:3$, $1:1 \ldots 4:7$ and those for $p \in [7,9]$ corresponds to $4:29, \ldots 4:35$, respectively.*

(a) Phasemap for constant amplitude $A = 0.5$.   (b) Phasemap for constant $p = 0.9$.
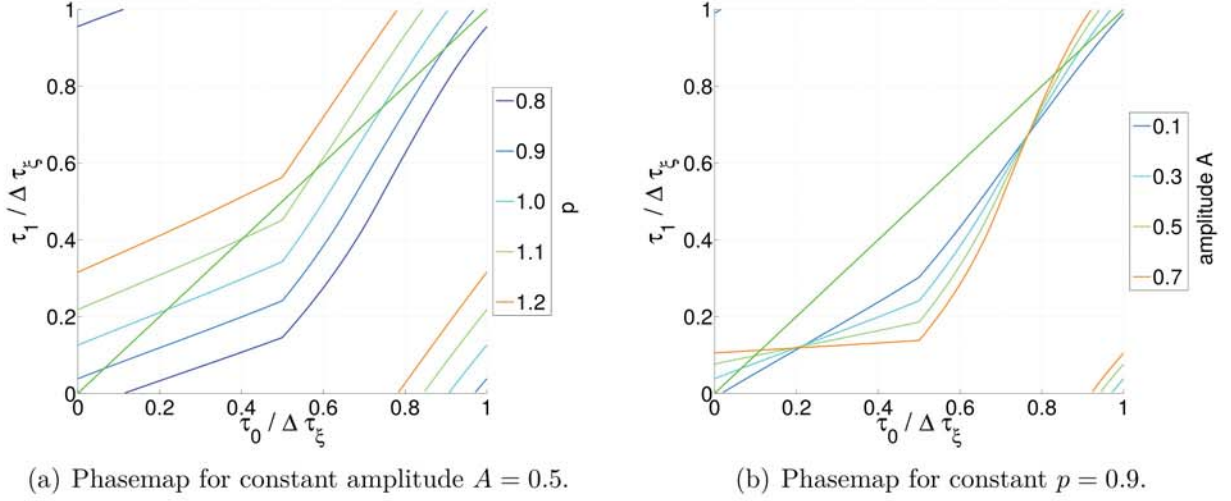
Figure 9: *Phasemap for (a) a fixed value of the amplitude $A = 0.5$ and different values of p and (b) a fixed value of $p = 0.9$ and different amplitudes.*

whereby $\tilde{\Phi}_0(\tau) = \tilde{\Phi}_{\tau_0=0}(\tau)$. The integration of the volume is independent of time and therefore Γ is constant. I assume the term $(\tau_1 - \tau_b)\,\tilde{\Phi}_0(\tau_0)$ to explain the qualitative behaviour of $\tau_1(\tau_0)$ in figure 9(b). First we know that for zero amplitude $\frac{d\tilde{\Phi}_0(\tau_0)}{d\tau_0} = 1$. In addition to that we know that $\frac{d\tilde{\Phi}_0(\tau_0)}{d\tau_0} = \tilde{\xi}(\tau_0)$. In case of square-wave or sinusoidal driving we therefore know that for $0 < A < 1$ and $\frac{\tau_0}{\Delta\tau_\xi} \in [0,0.5]$ one has $0 < \frac{d\tilde{\Phi}(\tau_0)}{d\tau_0} < 1$ and for $\frac{\tau_0}{\Delta\tau_\xi} \in [0.5,1]$ one has $\frac{d\tilde{\Phi}(\tau_0)}{d\tau_0} > 1$.

In case of constant driving ($A = 0$) we know that $\Delta\tau = const$ and thereby $\frac{d\tau_1}{d\tau_0} = 1$. Because $\Gamma := 3$ in equation (23) and $\tilde{\Phi}_0(\tau)$ and τ are positive a larger increase of $\tilde{\Phi}_0(\tau_0)$ ($\frac{d\tilde{\Phi}(\tau_0)}{d\tau_0} > 1$) leads to $\frac{d\tau_1}{d\tau_0} < 1$ which occurs for $\frac{\tau_0}{\Delta\tau_\xi} \in [0,0.5]$. For $\frac{\tau_0}{\Delta\tau_\xi} \in [0.5,1]$ we analogously get $\frac{d\tau_1}{d\tau_0} > 1$.

Starting from that I expect that the phase of the stable fixed points of period-1 Arnold tongues are always within the interval $[0,0.5]$ because otherwise the absolute value of the slope would be larger than one. Because for increasing p the curve $\tau_1(\tau_0)$ is shifted upwards the phase increases from 0 to 0.5 for increasing p and constant amplitude.

In first approximation I assume that the slope and thereby the range of p with synchronization is increasing linearly with increasing amplitude A. Therefore, I expect the width of the Arnold tongues increases linearly in dependence of the amplitude.

Secondly we observe in figure 9(b) that there are two phases τ_0 where τ_1 is nearly independent of the phase and all curves have a common intersection point. To explain this behaviour I assume that there is an intersection point $[\tau_0,\tau_1]$ of the curves for $A = 0$ and one arbitrary amplitude $0 < A_0 < 1$. Inserting equation (5) and $\tilde{\xi}(\tau) = 1 + A\zeta(\tau)$ in to equation

23

(23) for $A = 0$ and $A = A_0$ we conclude that

$$\int_{\tau_b}^{\tau_1} \int_{\tau_0}^{\tau} 1 \mathrm{d}\tau' \mathrm{d}\tau = \int_{\tau_b}^{\tau_1} \int_{\tau_0}^{\tau} 1 + A_0 \zeta(\tau') \mathrm{d}\tau' \mathrm{d}\tau \tag{24}$$

and thereby $\int_{\tau_b}^{\tau_1} \int_{\tau_0}^{\tau} \zeta(\tau') \mathrm{d}\tau' \mathrm{d}\tau = 0$. Hence, the curves $\tau_1(\tau_0)$ have a common intersection point independent of the amplitude A.

2.2.3 Width of period-1 Arnold tongues

In this section I will analyze the shape of the period-1 Arnold tongues, by examining the width and the asymmetry of the tongues on the p-axis in dependence of the amplitude A.

To precisely compute the left and right edges of the tongues we start from an uniformly distributed scan of the parameter space for $A \in [0,1]$ and $p \in [0,10]$. For each of the nine resulting period-1 Arnold tongue I examine the amplitude dependence of highest and lowest p that are still in the tongue. Beginning with those values I use nested intervals to approach the edge of the tongue with an accuracy of $\Delta p = \frac{1}{2^8}$. Based on those values more accurate left $l(A,n)$ and tighe border $r(A,n)$ of the n-th Arnold tongue I also calculate the midpoint $m(A,n) = \frac{l(A,n)+r(A,n)}{2}$ and the width $w(A,n) = r(A) - l(A)$ in dependence of the amplitude.

In figure 10 we see the left and right border of the fourth Arnold tongue ($n = 4$) in the p,A-space and the corresponding width and midpoint.
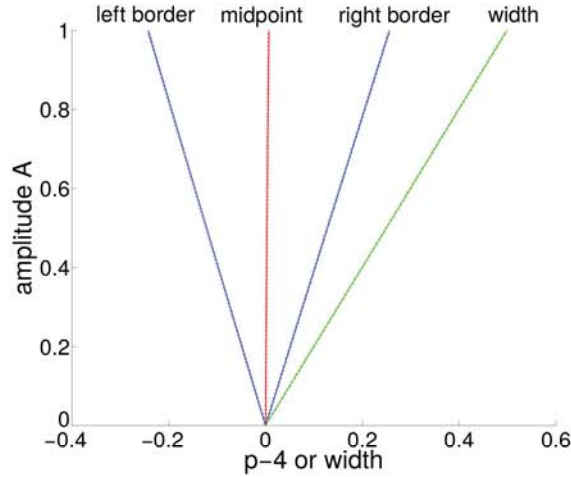

Figure 10: *Left and right border (blue) of the fourth period-1 Arnold and the the corresponding middle point (red) and the width (green) of the tongue in dependence of the amplitude A. For those dependencies I use a linear fit.*

Using the fact that the width of the tongues is zero for $A = 0$ I observe that for the left and right border a linear fit is a good description of the data. I therefore use *Matlab* to fit

$l(A,n) = n + l_0 A$ and $r(A,n) = n + l_0 A$ and compute the corresponding functions $w(A,n)$ and $m(A,n)$.

The calculated fit for the first tongue is indicated in figure 10.

I compute the fit parameters of the midpoint and the width for sinusoidal and square-wave driving for the first nine period-1 Arnold tongues to characterize the broadening of the tongues. Figure 11 shows the calculated values whereby the error of the fit parameter for the width are in the range of 10^{-4} to 10^{-3}.
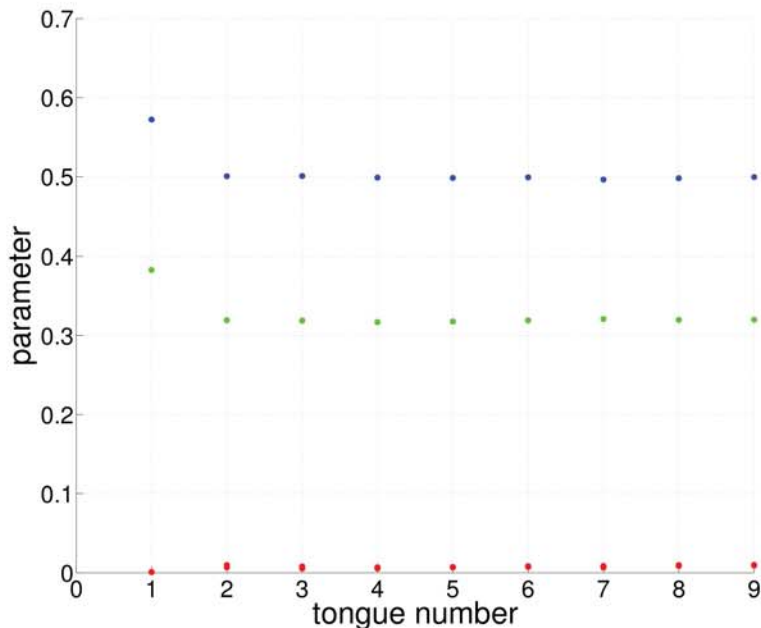
Figure 11: *Fit parameters for the first nine period-1 Arnold tonuges for the dependence of the width and the position of the midpoint from the amplitude. For the $n-th$ tongue I use the relation $m(A,n) = n + m_0 A$ for the midpoint and $w(A,n) = w_0 A$ for the width. The blue points show $w_0(n)$ for square-wave driving, the green points for sinusoidal driving, and the red points $m_0(n)$ for both cases. The error bars of the points are of the order of 10^{-4} to 10^{-3}, i.e. too small to be visible.*

The fit parameter of the midpoint is very small compared to the width of the period-1 Arnold tongues. Hence, there is no relevant asymmetry.

Due to this the expectation that the width is growing linearly in dependence of the amplitude is justified. We observe that the prefactor w_0 in case of square-wave driving is $w_0(1) = 0.572$ for the first tongue and $w_0(n > 1) = 0.498$ for larger tongue numbers which corresponds to a nearly constant broadening. For sinusoidal driving we see similar behaviour: $w_0(1) = 0.383$ and $w_0(n > 1) = 0.319$ for higher tongue numbers. Moreover, the curves appear to differ by a constant factor of the order of 1.5.

To make plausible that the tongues for the sinusoidal driving are narrower by a constant factor I consider $\tilde{\Phi}_0(\tau) = \int_0^\tau (1 + A\zeta(\tau')) \, d\tau'$. In case of sinusoidal driving I use

$\zeta(\tau') = \sin\left(\frac{2\pi\tau'}{\Delta\tau_\xi}\right)$ and for square-wave driving I use $\zeta(\tau') = -1$ for $\frac{\tau'}{\Delta\tau_\xi}$ [0,0.5] and $+1$ for $\frac{\tau'}{\Delta\tau_\xi}$ [0.5,1] due to the equations (18) and (19).

Integrating $\int_0^1 \zeta(\tau')d\tau'$ I get an amplitude (difference of maximal and minimal value) of the resulting function of $\frac{\Delta\tau_\xi}{\pi}$ for sinusoidal and $\frac{\Delta\tau_\xi}{2}$ for square-wave driving. Hence, we get a factor of about $\frac{2}{\pi}$ between the width of the tongues. Comparing both series of that parameter I gain a factor of about 1.49 for the first tongue and $1.564 \pm 0.006 \approx \frac{\pi}{2}$ between the width of square-wave and sinusoidal driving.

2.2.4 Phase of stable fixed points in period-1-cycles

In figure 12 I show the evolution of the phase for the first and the eighth tongue in case of square-wave driving.

As expected we observe that the phase of the fixed point is increasing from the left to the right border of the Arnold tongues from 0 to 0.5.
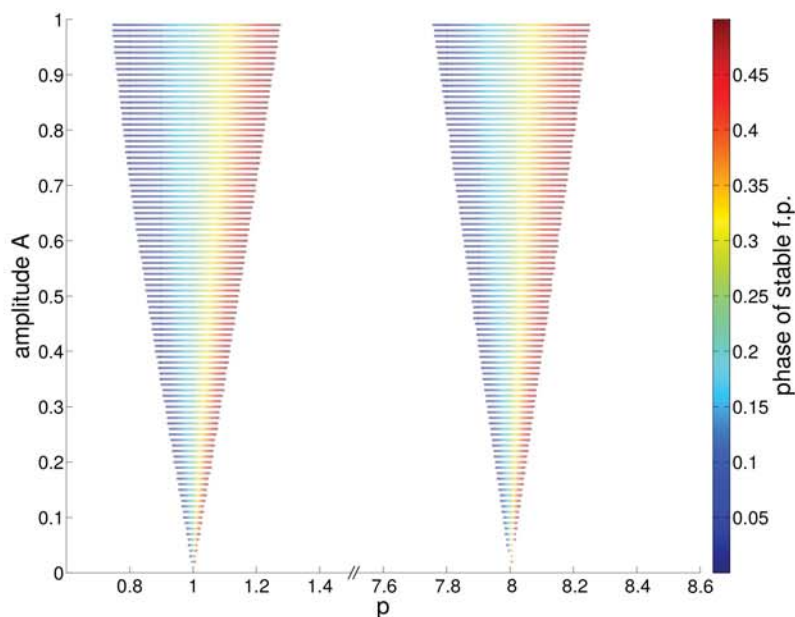
Figure 12: *Phase of the stable fixed point (f.p.) in the first and the eighth period-1 Arnold tonuge as a colormap for a square-wave driving. The phase is always in the interval [0,0.5] and thereby in the part with smaller driving.*

To analyze the behaviour of the phase in the tongues I show the dependence of the phase from the parameter p for a constant amplitude $A = 0.5$ in figure 13. For better comparision I shift the curves of the different tongues such that they are lying on top of each other. To obtain that I just draw the dependence of the phase from $p - n$ for the n-th tongue.

We observe that the phase is increasing nearly linearly from 0 to 0.5 whereby the curvature of the first tongue is larger (the second derivative is positive). This corresponds to a more frequent appearence of phases near 0.5. This is plausible because in case of square-wave driving (18) the time $\tau_b - \tau_0$ is minimal here due to the larger driving in the beginning.
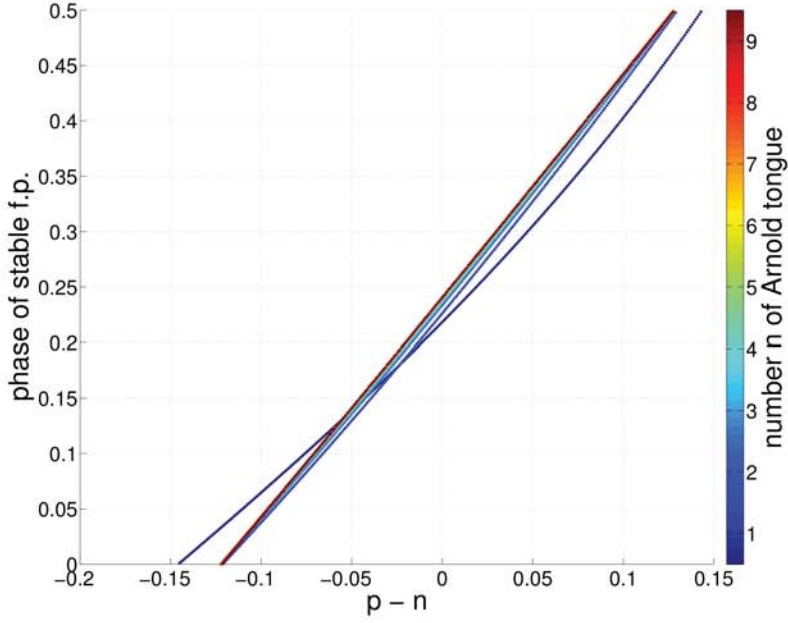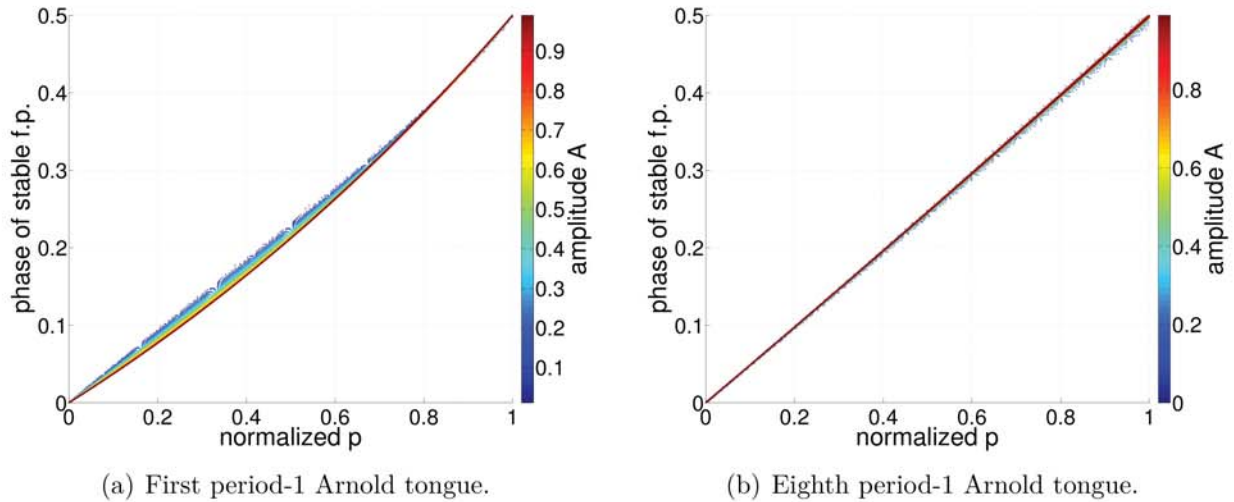

Figure 13: *The dependence of the phase of the stable fixed point in the first nine period-1 Arnold tongues. The tongues are shifted so that the integer values of p are lying on top of each other for comparision and they are color-coded to distinguish them.*

Additionally I show the dependence of the phase of the stable fixed point for the first tongues from the amplitude. In figure 14, I show the resulting phase in dependence of $p - n$ which is normalized to values from 0 to 1.

Analogously to figure 13 I see that the dependence of the phase from p is nearly linear and the curvature is larger for the first tongue than for the eighth tongue. Additionally I observe in figure 14(a) that the curvature increases slightly with growing amplitudes.

2.2.5 Second order Arnold tongues

In order to have a deeper look into Arnold tongues for square-wave driving corresponding to period-2-cycles I show the dependence of the phase for period-2 Arnold tongues in figure 15. I show the dependence of both stable fixed points on p and A for the tongue near $p = \frac{1}{2}$ and $p = \frac{3}{2}$. In this case the phase of the smaller fixed point is in the interval $[0,0.5]$ and the phase of the larger fixed point in the range of 0.5 to 1. Moreover, to the period-1 Arnold

(a) First period-1 Arnold tongue.

(b) Eighth period-1 Arnold tongue.

Figure 14: *Dependence of the phase of the stable fixed point in period-1 Arnold tongues for different values from a normalized p and the amplitude. For each amplitude and tongue p is stretched such that the width of the tongue is 1 and the left border corresponds to 0 and the right border to 1. The dependencies for different amplitudes are marked with different colors.*

tongues above the phase is increasing from the left to the right borders of the period-2 Arnold tongues.

Moreover, the second tongue is much smaller than the first tongue, and there is a drift to smaller p for the first tongue.

2.3 Discussion

Remarkably, my numerical results do not fit the experimental observations. At least there is the similarity that we observe synchronization and phase locking in both the experiments and the numerical model.

In order to explore how my numerical results compare to experimental observation on synchronization I compare them now to data obtained by Julian Vogel in his bachelor thesis [22]. He observed the turbidity of the sample of a iBE/water system subjected to square-wave driving to examine whether there is synchronization for specific p and A. The turbidity increases if more droplets are present.

Firstly Julian observed phase locking in a period-1-cycle for $p = 1$ and several different amplitudes A up to 12 succeding periods of episodic precipitation. It may be noted that experimental constraints prevent measure of periods because the sample reaches the maximal temperature of the setup of about 50 °C. Julian observed a phase of about 0.8 which lies in the regime of larger driving ξ for the time of minimal turbidity and thereby the begin of the next precipitation cycle. There is good case to believe that this phase of minimal turbidity
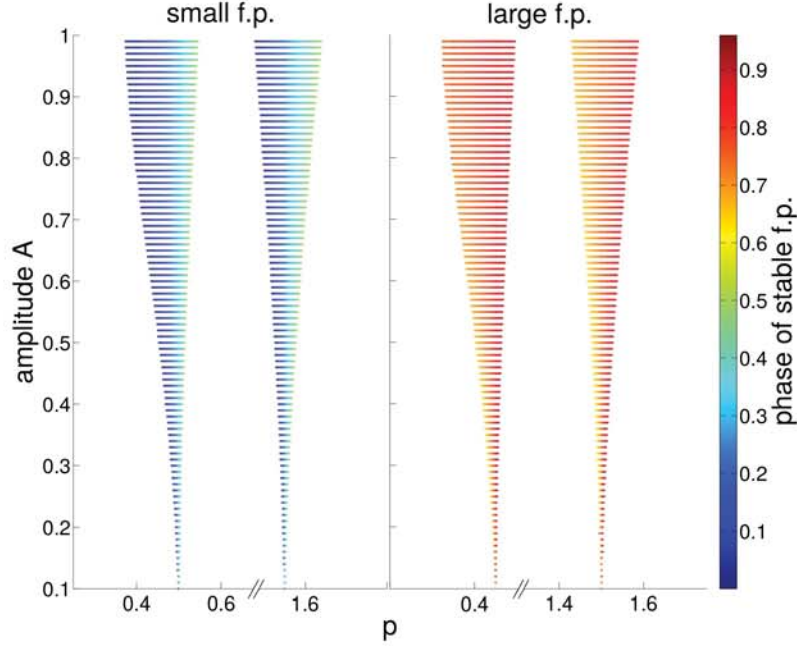
Figure 15: *dependence of the phases of the two stable fixed points in period-2 Arnold tongues. In the left plot the phase of the smaller fixed point of the tongues at $p = 1/2$ and $p = 3/2$ are and in the right plot the larger f.p. is shown. Note that the scale of the p-axis is constant and partially interrupted.*

does not coincide with the phase of the nucleation of the droplets in my model. The turbidity is not increasing until the droplets approach radii of several hundred nanometer where they scatter visible light. Because of that I assume that the phase of nucleation is slightly before the phase of minimal turbidity which does not explain the deviations regarding my numerical results where the phase of nucleation is always in the regime of smaller driving. This leads to the question how to explain this deviation.

Secondly Julian observed frequency locking in case of $p = 0.89$ and $A = 0.1$, $p = 0.81$ and $A = 0.2$ for about 4 to 5 periods. Due to the fact that there are phase slips in those cases it is probable that the synchronization is not stable here. Additionally he observed a 1 : 1 synchronization for $p = 0.5$ and $A = 0.5$ for about 5 periods and possibly a 2 : 1 synchronization in case of $p = 1.5$ and $A = 0.5$ for about 7 periods. The latter case is doubtful due to some smaller peaks of turbidity between the major peaks. In contrast there is no period-1-cycle in my numerical results for those four cases which lie far outside of the period-1 Arnold tongues. I emphasize especially the measurements for $p = 0.5$ and $p = 1.5$ because my results would predict period-2-cycles.

Actually I would expect even thinner and not broader Arnold tongues because in the experimental realization intended square-wave driving is flattened due to the slackness of

the thermostat: Due to the fact that the computed Arnold tongues for sinusoidal driving are much thinner I expect that flattened square-wave driving would lead to a width in between square-wave and sinusoidal driving.

In equation 14 we see that the model for droplet growth has no dependence on specific parameters. Therefore the comparision above suggests that the model, which only predicts the growth of the characteristic large droplets, is not sufficient to describe episodic precipitation with time-dependent driving and thereby the droplet growth in cases of time-dependent driving.

This result motivates me to experimentally investigate the effect of diffusion, coalescence and sedimentation on a more fundamental level: I detect single droplets and their radii to evaluate the droplet size distribution. To avoid non-essential complexity I run simplied temperature ramps with only a single decrease of driving.

3 Evolution of droplet size distributions

In this chapter I will present my experimental results of the evolution of droplet size distribution subjected to a nontrivial step-like driving, $\xi(t)$, shown in figure 17(a) especially for negative driving. I use a model system of iso-butoxyethanol (iBE) and water in a small test-tube as described in section 1.3.

In section 3.1 I present the experimental and numerical procedure which is used to determine the evolution of the droplet size distributions for different types of temperature ramps in section. I discuss the experimental setup, the measurement protocol and sketch the algorithm used to detect droplets in the acquired images. The emphasis of this discussion is on problems in the experiment and the data analysis.

In the beginning of my project I made a few test measurements to analyze episodic precipitation by observating the turbidity in the sample with the dark-field setup described in [22, 12]. After some efforts to develop an experimental setup [11, 13, 20] which allows us to observe turbidity and single droplets simultaneously Martin Rohloff and I revived the setup developed by by Martin Rohloff and Tobias Lapp to analyze single droplets. I adapted the software and computed specific temperature ramps to use them in the experiment. To analyze the images and detect single droplets I adapted the *Matlab* scripts developed by Lapp and Rohloff. I changed the scripts and varied a number of parameters in the algorithm to optimize the detection of single droplets.

Secondly I will examine episodic precipitation for a temperature ramp corresponding to a positive, constant driving to reproduce the studies from Martin Rohloff et al. [20]. After that I will show the characteristic behaviour of the evolution of droplet size distributions for constant and decreasing temperatures after evolving a size distribution through positive driving for a specific time. At last I will try to describe a model to collapse those evolutions.

During my thesis I made about 50 measurements corresponding to different times for the heating and either negative or zero driving after it.

3.1 Experimental approach

3.1.1 General measurement procedure and setup

The main part of the experimental setup where the demixing of the binary fluid and the nucleation and merging of droplets occurs is a flourescence cell *117.100F-QS* with a size of $10 \times 10 \times 35\,\mathrm{mm}$ by *Hellma GmbH*. After cleaning the cell with destilled water and getting rid of small water droplets through ventilation with compressed air we pipette a defined amount of water and iBE into the cell near the composition of the critical point in figure

3(a). We pour in an overall volume of 2 ml with about 30 volume percent of a mixture of iBE and the flourescent dye nile red. The exact composition is computed by weighing the cell using a scale with an uncertainty of 0.0001 g. Subsequently we add a small stirring bar (about 6 mm length and 3 mm diameter) for later homogenization the binary fluid, and seal the cells with teflon tape to ensure that no water is invading.

Nile red absorbs light primarily in a wavelength interval of 500 to 590 nm (green or yellow light) and emits this light due to flourescence in the interval 580 to 700 nm which corresponds to orange/red light. The influence of the dye being in solution on the phase diagram depicted in figure 3(a) is negligible (see [11, 20]). The flourescent dye nile red is dissolved in the iBE near complete saturation to increase the contrast between the two separated phases in order to enable the detection of droplets. The dye is preferentially soluble in the iBE-rich phase and therefore droplets of the iBE-rich phase will be brighter than the water-rich background if illuminated with an appropriate light source.

The measurement cell is mounted at the edge of a water bath filled with destilled water of a size of $14 \times 34 \times 16$ cm and a controlled temperature. The cell is attached to a shift mechanism in a manner that we can control the position in all three directions with micrometer screws. The large size of the water bath should reduce unintended variations of the temperature on small time scales and is needed for the cooling device and the thermostat. On that account we use a *Haake EK20* immersion cooler which is running all the time with a constant power of 300 W. The cooling coil is mounted within the water bath and the cooler itself on a second table to reduce vibrations which were disturbing the detection of single droplets. Moreover a *Huber CC-E* immersion thermostat is used to control the preset temperature. Precise temperature measurements near the sample were taken with a *PT100* temperature sensor. The thermostat is provided with a pump to circulate the water, and spatially homogenize the temperature in the water bath. To avoid vibrations we have to restrict the strength of the pump to the minimal possible value of 1500 rpm. In order to automatically homogenize the sample before and in between measurements we place the magnetic stirrer *IKAMAG RET control-visc C* below the bath under the measurement cell. It allows stirring rates from 50 to 1500 rpm.
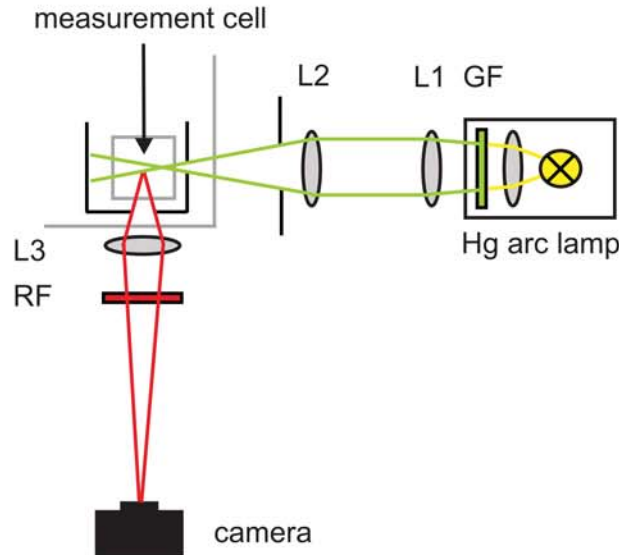
3.1.2 Optical setup

The droplets in the sample are illuminated through a thin and vertical slit with a bright, green mercury short arc lamp (Hg-light source) from *LOT-Oriel* and a power of 100 W at an angle of 90 deg relative to the observance angle. Figure 16 shows a sketch of the optical setup and the cell. The lamp has emissions lines of 546, 577 and 579 nm.[4] The light is

---

[4]see: http://physics.nist.gov/PhysRefData/Handbook/Tables/mercurytable2.htm

first collected by a collimator lense C. Then a green band-pass filter GF (*FF01-562/40-25*) by *Semrock* allows only the double line 577 and 579 nm to pass which lies in the excitation band of nile red. After that a spherical lens L1 ($f = 200\,\text{mm}$) and a cylindrical lens L2 ($f = 80\,\text{mm}$) are focusing the light to attain homogenous illumination of maximum intensity on the thin slit where we measure a focus width of about 2 mm and a height of 4 mm.

Figure 16: *Sketch of the optical setup. The light from a Hg arc lamp is firstly collected by a collimator lense (C) and is passing a green-filter (GF). After that the light is focused with a spherical and a cylindrical lense (L1 and L2) and is reaching the measurement cell within the water bath through a thin slit. The CCD camera is observing the flourescent light in the sample through a zoom lense (L3) and a red-filter (RF). The figure is adapted from [11, 13].*

The sample is observed using the CCD camera *BM-500CL*[5] which is mounted with a micrometer screw adjustment and has a resolution of $2456 \cdot 2048$ pixel. Starting from the measurement cell the light has to pass a circular aperture with a radius of about 2.8 mm a zoom lens L3 and a long-pass red filter RF by *Semrock* (*BLP01-594R-25*) only which allows the emitted light of the flourescent dye to pass. Length scales in the images are calibrated by a caliper: I measure the distance I have to move the measurement cell to change the position of a specified point in the gathered image about some range, and compute the conversion factor between real size in the sample and pixels in the images, yielding a resolution of $1.7(1)\,\frac{\text{px}}{\mu\text{m}}$.

The observation with the camera takes place in the bottom layer of the measurement cell, i.e. in the water-rich phase where the nucleated droplets are iBE-rich and thereby show brighter flourescence. The contrast between the droplets and the surrounding phase

---

[5]see: http://www.jai.com/en/products/bm-500cl

makes it possible to observe single droplets. The thin slit with a width of about $100\,\mu$m[6] on a black plate is mounted directly in front of the measurement cell within the water bath. The position of the measurement cell is adjusted in a way that the thin slit effects in an illuminated plane in the front of the cell looking from camera direction. If we would observe a plane which has a larger distance from the wall the emitted flourescence light would have to cross many droplets and would thereby be scattered such that we cannot reliably trace individual anymore.

I use a *LabVIEW* programm to enable automated measurements where we control the thermostat, the magnetic stirrer, the light source and the camera. I adapt the program to run my own temperature ramps.

3.1.3 Data acquisition

The *LabVIEW* programm performs the following tasks:

- Mix the binary fluid using the stirring bar at 1500 rpm and a temperature of about 23 °C $< T_c$ for about 60 min. After this time the fluid is homogenized.

- For about 180 min the temperature is kept constant at least 0.2 K above the transition temperature. Hence, the phases seperate macroscopically and reach equilibrium.

- The light source is switched on, a temperature ramp is run and image acquisition begins using a constant frame rate of about 500 mHz. During the measurement *LabVIEW* is logging the temperature of the thermostat and the *PT100* sensor for later control of the temperature ramp.

It occurs that there is a significant and systematic shift of transition temperatures relatively to the theoretical transition temperatures corresponding to the actual composition from figure 3(a). I assume that the phase diagram is just constantly shifted by this temperature difference.The causes may be impurites within the used iBE or a systematic shift in the measurement of the temperature. To adjust the computed temperature ramps I thereforehave to determine the occurring temperature shift T_{shift} for every sample [13].

The transition temperature is determined through slow heating with maximum stirring rate and direct observation. I estimate an occurring uncertainty of about 0.1 K. It can be seen clearly when the droplets are emerging because the binary fluid is getting turbid rapidly. We have to observe this directly because a more accurate measurement of the turbidity is not possible with the mounted setup. A determination through the droplet size distribution is unconvenient because in the beginning the nucleated droplets are far too small to detect.

---

[6]I measured the width of the slit using diffraction of laser light.

3.1.4 Temperature ramps

In our model system we induce phase seperation by changing the temperature of the sample. In this section I show my approach to determine temperature ramps which generate specific time-dependent driving $\xi(t)$ [1, 13, 20].

Let φ_l and φ_r denote the fraction of iso-butoxyethanol in the left and right branch of the phase diagram respectively. Hence, the half width of miscibility gap in the phase diagram 3(a) is

$$\varphi_0(T) := \frac{\varphi_r(T) - \varphi_l(T)}{2}. \tag{25}$$

According to the lever rule in Maxwell's theory of phase coexistence a temperature ramp results in the following change of the droplet volume fraction for the bottom layer:

$$\xi = \frac{1}{2\varphi_0(T)} \frac{\mathrm{d}\varphi_l(T)}{\mathrm{d}t}. \tag{26}$$

Using the chain rule $\frac{\mathrm{d}\varphi_l(T)}{\mathrm{d}t} = \frac{\mathrm{d}\varphi_l(T)}{\mathrm{d}T} \frac{\mathrm{d}T}{\mathrm{d}t}$ the slope of the temperature ramp is given by:

$$\frac{\mathrm{d}T}{\mathrm{d}t} = \frac{2\xi(t)\varphi_0(T)}{\frac{\mathrm{d}\varphi_l}{\mathrm{d}T}}. \tag{27}$$

Starting from this differential equation we obtain the ramp $T(t)$ by numerical integration of (27) using Euler-stepping.

To analyze the effect of large amplitude $A > 1$ which corresponds with intermittently negative driving $\xi(t)$ on the evolution of droplet size distribution I use simplified temperature ramps to gain basic understanding of the effects of $\xi(t) < 0$ and the thereby occurring shringing and evaporation of droplets.

First I use temperature ramps with a constant driving $\xi(t) = \xi_A = 2.5 \times 10^{-5}\,1/\mathrm{s}$ for a long time $\Delta t_A = 2 \times 10^4\,\mathrm{s}$ to enable comparision of the effects of negative and positive driving.

Figure 17(a) shows the temperature ramp for a characteristic time-dependent driving $\xi(t)$. Beginning with a positive driving of ξ_A for a time of Δt_A the driving jumps to the value $\xi_B < 0$ which will lead to shrinking and evaporation of droplets. The first part corresponds to an increase and the second part to a decrease of temperature because the slope of $T(t)$ is proportional to $\xi(t)$. The time Δt_B of the second part is choosen long enough that all droplets are vanished at the end of the measurement.

In figure 17(b) I show an exemplary comparision between an intended and the obtained temperature ramp $T(t)$ measured by the PT100. The experimental data nicely follows the desired temperature evolution. The variations of the measured values of the *PT100* are

(a)　　　　　　　　　　　　　　　　　(b)
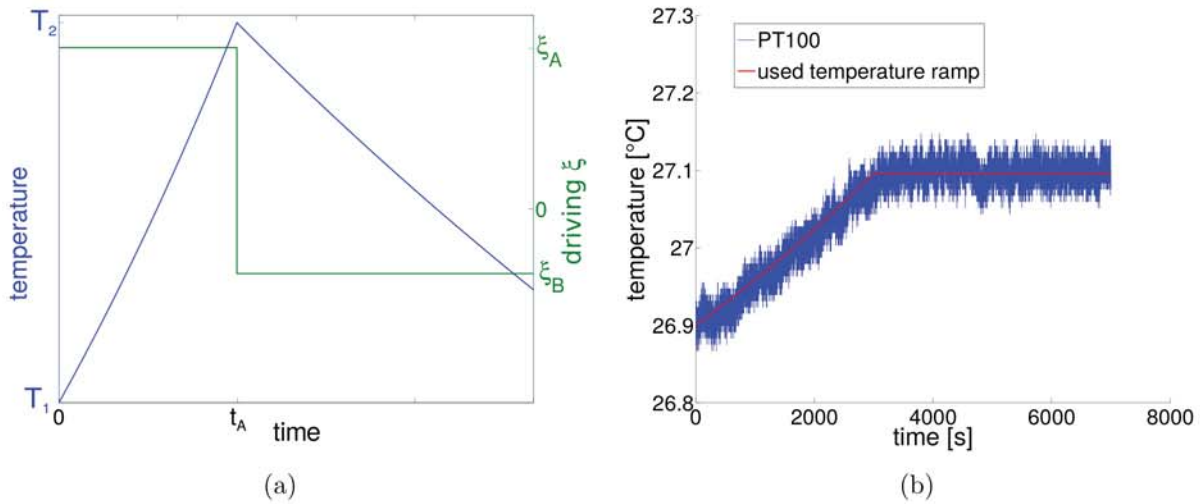
Figure 17: *(a) Temperature ramp for time-dependent driving. The temperature $T(t)$ (blue) is increased from T_1 to T_2 with a driving of $\xi(t) = \xi_A$ in the time-interval $[0, t_A]$. In the second part a non-positive driving ξ_B is used and the temperature is decreasing. (b) Exemplary comparision of the intended (red) and the obtained temperature ramp (blue) measured by the PT100.*

about $0.02\,\mathrm{K}$.

3.1.5 Droplet detection

In this section I consider the algorithm to detect single droplets in the image sequences. Except for small modifications the algorithm developed by Tobias Lapp and Martin Rohloff is used as introduced in [13, 11, 20]. I use and adapt their *MATLAB* scripts to preprocess the images and to analyze the radius and the position of the single droplets. Because there are at least 4000 images per measurement the scripts are run on the Cluster of the Max-Planck Institute for Dynamics and Self-Organization.

Because of the complexity of the algorithm I will only sketch the approach which is described in more detail in [13]. Firstly the acquired images are preprocessed to get images where the droplets are visible more clearly to enable the algorithm to find them. In figure 18(a) we see an exemplary image before and in 18(b) we see this picture after preprocessing.[7] Starting from that preprocessed image two methods are used to find potential droplet candidates. We observe that far too many droplet candidates are noticed. Therefore we have to define a measure[8] of the quality of a candidate based on the image – candidates where this

---

[7]In contrast to Lapp et al. who uses $\sigma = 100$ for the isotropic, low-pass Gaussian filter I use $\sigma = 40$ to get rid of significant part of the noise.

[8]Within this measure Lapp uses the intensity within a ring of $3\,\mathrm{px}$ (pixel) around the droplets. In contrast to that I use a radius-dependent ring-width of $W(r) = 3\,\mathrm{px} + 0.1r$ because larger droplets are empirically detected better herewith.
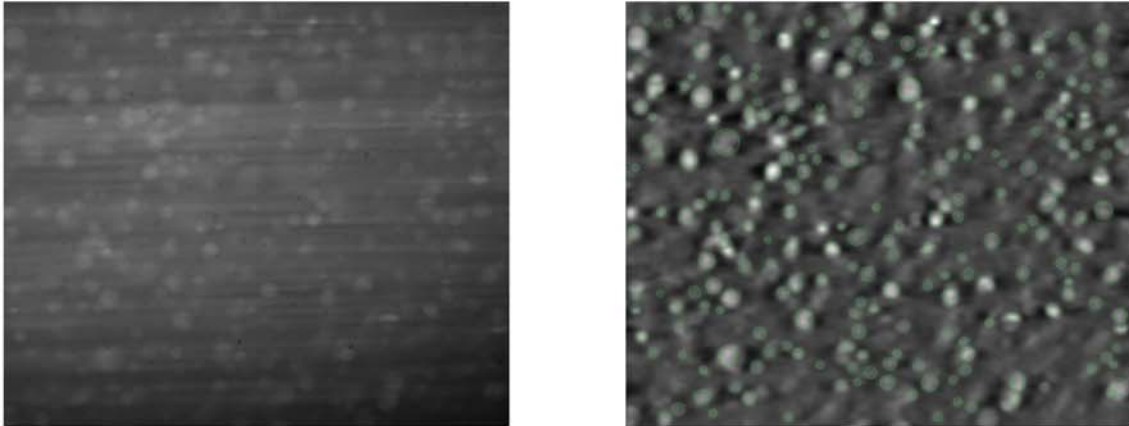
(a) Raw image before preprocessing.   (b) Image after preprossing with detected droplets.

Figure 18: *Exemplary image from the bottom layer where the droplets are iBE-rich.*

matching value exceeds a threshold[9] are seen as droplets. [10]

In figure 18(b) I show the detected droplets. I note that I cannot sufficiently detect droplets with radius smaller than the minimal radius $r_{\min} \approx 8\,\text{px}$ and therefore I only consider detected droplets if they are larger. Above this threshold most of the droplets are detected and there are only a few false positives. Due to Rohloff we obtain a relative uncertainty of about 20% for $r < 20\,\mu\text{m}$ and about $4\,\mu\text{m}$ for larger droplets [20, p. 41].

---

[9]In contrast to that Lapp et al. who delete all droplets which do not reach the threshold 0.08 I choose 0.06.

[10]In many images we observe that there are small droplets at the edge of larger droplets which cannot be seen in the image although they exceed the threshold. Because this problem is just occurring at the edge of droplets I delete the small droplets whose centre is inside a larger droplet to reduce that error uncertainty in droplet size distribution.

3.2 Evolution of droplet size distributions with time-dependent driving

3.2.1 Calculating droplet size distributions

Important characteristics of droplet size distributions are the droplet volume and the droplet number density per radius. The droplets are detected in the focus plane of the camera,i.e. in a clearly defined area A which is given by the image size. To determine the depth of the detection volume it is not sufficient to take the width of the thin light sheet used for droplet illumination, which is about $100\,\mu$m which because I am not able to detect all droplets within this volume: On the one hand the depth of the focus plane is smaller than the width of the light sheet. On the other hand droplets may be behind one another. Following Tobias Lapp I hence assume that the probability to detect droplets of a radius r is proportional to that radius. To compute the depth he uses $d = \frac{1}{4r}$[11, p. 101] and therefore I obtain the overall droplet number and volume density $n(t)$ and $v(t)$ corresponding to an image at the time t by

$$n(t) = \sum_i \frac{1}{4r_i A} \qquad \text{and} \qquad v(t) = \sum_i \frac{1}{4r_i A}\frac{4\pi\, r_i^3}{3} = \sum_i \frac{\pi r_i^2}{3A} \tag{28}$$

where r_i is the radius of the i-th droplet detected in the field of view of the sample area A.

These droplet number densities should be considered as a lower estimate of the real values. Lapp estimated, $d = \frac{1}{4r}$, is an upper limit of the depth, and because I do not detect droplets smaller than $r_{\min}$ and there are only a few false positives.

To investigate the time evolution of droplet size distributions I use a representation of a two-dimensional histogram. I use linear time bins with a duration of $100\,$s which corresponds to 50 images and 20 logarithmic radius bins from $8\,$px $\,\hat{\approx}\, 5\,\mu$m to $80\,$px. Smaller droplets are not detected accurately, and only rarely there are larger droplets occurring. To compute the droplet number density for radius bin $[R_{k_1}, R_{k_2}]$ for an image I use

$$n_r(R_k,t) = \sum_{\substack{i,\\ R_{k_1} < r_i < R_{k_2}}} \frac{1}{4r_i A}\frac{1}{R_{k_2} - R_{k_1}}. \tag{29}$$

After that I average the number densities for all acquired images in one time bin which is necessary to reduce the noise in the signal. Effects on $n_r(r,t)$ appearing on time scale s smaller than $100\,$s will not be resolved.

3.2.2 Characteristic velocities in the model system

In the model described in section 1.4 the droplets with radius larger than the bottleneck radius r_b experience sedimentation and growth by coalescence. Lapp estimates that r_b for

the water/iBE-system will be about $10\,\mu$m, and he measured the collision efficiency to be 1 to 3% for smaller radii[11, p. 90]. Using equation (3) I calculate the sedimentation velocites for temperatures of about $27\,°C$ which are typical in my temperatures ramps: Small droplets with $r \approx 1\,\mu$m have a sedimentation velocity of about $u_{\text{sed}} \approx 0.07\,\frac{\mu\text{m}}{\text{s}}$, droplets with $r \approx 10\,\mu$m of about $u_{\text{sed}} \approx 7\,\frac{\mu\text{m}}{\text{s}}$, and for $r \approx 30\,\mu$m one finals $u_{\text{sed}} \approx 60\,\frac{\mu\text{m}}{\text{s}}$. Characteristic droplet sizes in my measurements lies in the regime of $5\,\mu$m to 20-40 μm.

Because of temperature gradients there is a convective cell in the bottom layer of the test tube which features turnover velocities of the flow field of about 5 to $20\,\frac{\mu\text{m}}{\text{s}}$ [20, p. 50]. The flow runs downward in the window for image sequences observing the bottom layer: Hence, I find that larger droplets move upwards due to sedimentation while small droplets are advected downwards. A comparision of the sedimentation velocities and the velocities of the flow field suggests that both velocities are of the same order of magnitude.

To estimate the time scale of a complete demixing of the system I use the typical flow field velocities of about $10\,\frac{\mu\text{m}}{\text{s}}$, and a length scale of the test tube of about $1\,$cm. This leads to time scale of $1000\,$s which is in the order of magnitude of the precipitation periods in episodic precipitation. Consequently, nucleated droplets are transported throughout the complete sample during one precipitation cycle.

To examine whether small scale turbulences lead to relevant effects in the model system I estimate the Reynolds-Number using

$$Re = \frac{\rho v d}{\eta} \approx \frac{\rho\, u_{\text{sed}}\, r}{\eta} = \frac{\rho\, \kappa\, r^3}{\eta} \tag{30}$$

where d denotes a characteristic length scale of a moving object with velocity v. η is the viscosity and ρ the density of the surrounding fluid. For temperatures of about $27\,°C$ I obtain $Re \approx 2 \times 10^{-3}$ and for $40\,°C$ I get $Re \approx 8 \times 10^{-3}$. Both values are several orders of magnitudes smaller than critical Reynolds number which are in the order of the magnitudes of 1000. Therefore we do not have to consider turbulences on small spatial scales – which I additionally do not see in the image sequences – in the model.

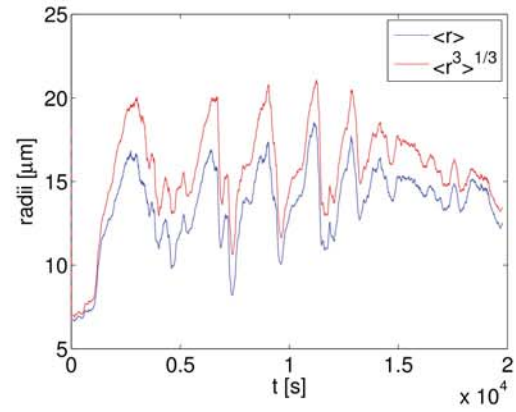### 3.2.3 Evolution for constant driving

In figure 19 I show experimental results for a temperature ramp corresponding to a constant driving $\xi(t) = 2.5 \times 10^{-5}\,\frac{1}{\text{s}}$ for a time duration of $2 \times 10^4\,$s. The sample volume is about $3\,$ml the height of the meniscus is at about $1.5\,$cm.

In figure 19(a) we see the overall droplet volume fraction in the system. The density is zero in the beginning because measurements started in a phase-sperated equilibrium state where there are no droplets. Subsequently it features repeated minima and maxima, of about $1.5\,\%$
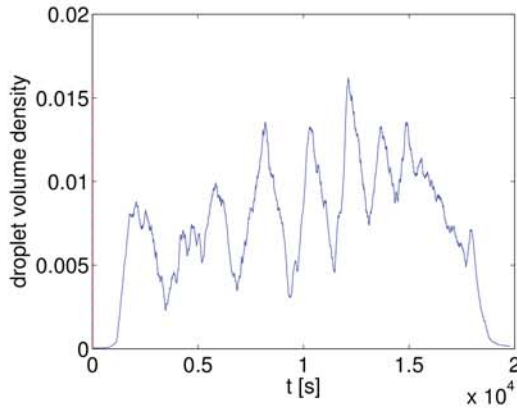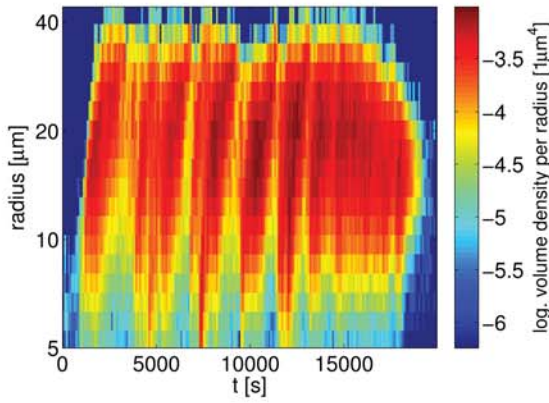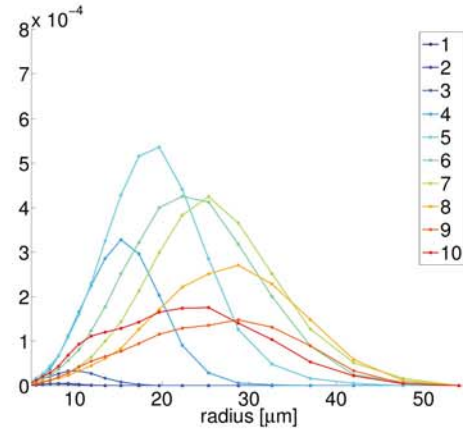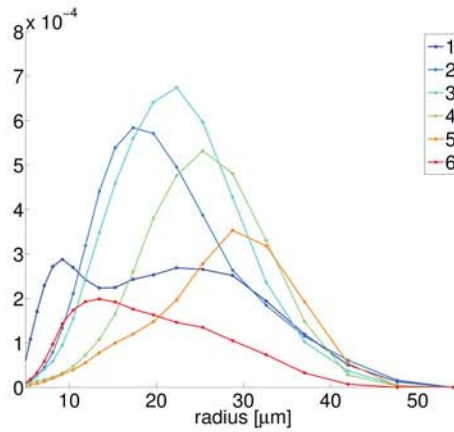
(a) Evolution of the droplet volume density

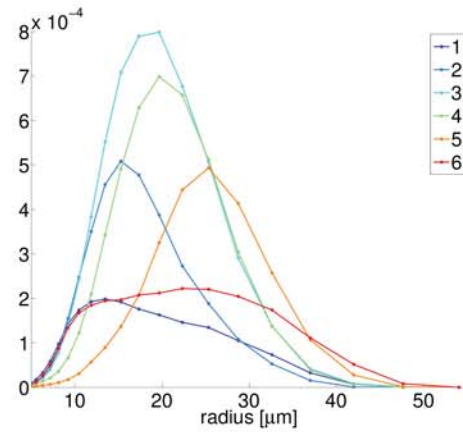(b) Evolution of the mean radii of droplets

(c) Evolution of the droplet volume density

(d) Volume density from 200 s to 3400 s

(e) Volume density from 7600 s to 9600 s

(f) Volume density from 9600 s to 11 600 s

Figure 19: *Measurement for a constant driving $\xi(t) = 2.5 \times 10^{-5}\, \frac{1}{s}$ for about 20 000 s. (a) The overall droplet volume density in dependence of the time. (b) I show the mean radii $\langle r \rangle$ and $\langle r^3 \rangle^{1/3}$. (c-f) I show the droplet volume density per radius and time bins: (c) The image show the two-dimensional histogram for all 20 radius and 200 time bins. (d-f) The images show the evolution of droplet volume distribution during single precipitation events whereby I average over four time bins (400 s) for each curve and over three of the 20 radius bins to smooth the curves. Between the color-coded lines is a constant time of 400 s. The images corresponds the first, third and fourth precipitation event.*

40

near the maxima. There are seven peaks within the first $1.5 \times 10^4 \, \mathrm{s}$ with decreasing period. After this time the volume density has no clear peaks anymore. I attribute the oscillations to episodic precipitation with a period of about $2000 \, \mathrm{s}$.

In figure 19(b) I show the mean radii $\langle r \rangle$ and $\langle r^3 \rangle^{1/3}$. We observe seven maxima in that time, too, and see that the mean radius $\langle r \rangle$ is fluctuating between $10 \, \mu\mathrm{m}$ and $17 \, \mu\mathrm{m}$ except for the beginning where are only small droplets. At this point it is important to note that we detect only droplets larger than $r_{\min} \approx 5 \, \mu\mathrm{m}$. Therefore the mean radius $\langle r \rangle$ of the droplets must be larger than $r_{\min}$, and it overestimate $\langle r \rangle$. Because of this I also show $\langle r^3 \rangle^{1/3}$ because the neglection of smaller droplets has a smaller effect on this value. It is more robust regarding the minimal radius. This value lies during except for the beginning in the interval from about $12 \, \mu\mathrm{m}$ to $20 \, \mu\mathrm{m}$.

We see that $\langle r^3 \rangle^{1/3} > \langle r \rangle$ because larger droplets have more weight in the first term. In the course of the precipitation events both values show a similar behaviour. The mean radii are nearly constant for later times which is consistent with the observation that we cannot distinguish possible precipitation events in figure 19(a), too.

The mean radius is characteristically increasing slightly after the increase of the overall volume fraction. This is plausible due to collection: Large droplets are collecting smaller droplets whereby the volume density is constant but the number of droplets is decreasing thereby the mean volume and $\langle r^3 \rangle^{1/3}$ is increasing.

In figure 19(c) I show a two-dimensional histogram of the droplet volume density per radius for the complete duration and 20 radius bins. We observe the precipitation events, too and see that the regimes of larger droplet volume density go off slightly skewed to larger radii. This corresponds to the increase of the characteristic radii during the precipitation events.

In figure 19(d) to 19(f) I show the evolution of the droplet volume density per radius for single precipitation events for deeper insights:

Figure 19(d) shows the beginning of the measurement and the first oscillation: At early times there are no droplets and after $400 \, \mathrm{s}$ we observe that there is a small peak in the regime of $10 \, \mu\mathrm{m}$ (dark blue). During the following $800 \, \mathrm{s}$ the droplet volume density is increasing rapidly and the maxima of the distribution is shifting to a radius of about $20 \, \mu\mathrm{m}$ (light blue). After that we see an reduction of the droplet volume density and a further shifting of the maximum of the distribution to about $30 \, \mu\mathrm{m}$ (yellow). Following further reduction of the density with constant maxima we observe that the number of smaller droplets is beginning to increase rapidly and the distribution is shifting towards smaller radii.

To explain this behaviour I have a look on the diffusional growth in equation (2). Using typical droplet number densities of about $0.5 \times 10^{-6} \, \mu\mathrm{m}^{-3}$ and $\xi(t) = 2.5 \times 10^{-5} \frac{1}{\mathrm{s}}$ I compute

$\dot{V} \approx 5\,\frac{\mu\mathrm{m}^3}{\mathrm{s}}$ which corresponds to $V \approx 5000\,\mu\mathrm{m}^3$ after $1000\,\mathrm{s}$, corresponding to droplet radii of about $10\,\mu\mathrm{m}$. And after another $1500\,\mathrm{s}$ they grew to $14\,\mu\mathrm{m}$. Subsequently, diffusional growth can no langer account for the observed large droplet volume.

In the beginning we observe that droplets are growing by diffusion and thereby reach radii of about $10\,\mu\mathrm{m}$ but to explain radii of $25\,\mu\mathrm{m}$ in further evolution about 10 droplets with a radius of about $15\,\mu\mathrm{m}$ have to merge due to collection whereby diffusion would not be able to explain this behaviour.

I attribute the observed growth by collection to collection of smaller droplets which are not detected because there is no noticeable reduction of droplet volume density per radius for the observed droplets.

In the further evolution large droplets sediment and rapidly are increasing in size due to collection. Eventually, all visible droplets are sedimented, and a new cycle of nucleation, subsequent growth by diffusion and collection, and sedimentation starts. Eventually the volume density is therefore decreasing while the size of characteristic large droplets is increasing.

When the next cycle is beginning, small droplets have to come into being by the demixing in the sample. The turnover time scale of the convection is on the order of magnitude of about 1000 to $1500\,\mathrm{s}$, such that the flow disperses the small droplets homogenously in the sample even when they come forth by heterogeneous nucleation or compley process at the interface during sedimentation.

In figure 19(e) we see a similar evolution for another precipitation event. It may be noted that there is a bimodal distribution in the beginning. At time $t = 7600\,\mathrm{s}$ it occurs that large droplets of the previous event are not sedimented yet while small droplets of the next precipitation already reach a relevant volume density. This means that the events are overlapping in time and therefore we never see that all droplets are vanishing again.

In figure 19(f) I show the next cycle shows a similar evolution. Our observation of single precipitation events is robust, and not occurring by luck one time.

3.2.4 Evolution for non-positive driving

In the following I will study the evolution of droplet size distributions in case that there is no positive driving but either a constant temperature and thereby zero driving or negative driving. The experiments are performed using a starting temperature of $26.9\,°\mathrm{C}$ (The measured temperature shift of $T_{\mathrm{shift}} = 0.9\,°\mathrm{C}$ is included.) and using an overall volume of about $2\,\mathrm{ml}$ which corresponds to a height of the meniscus of about $1\,\mathrm{cm}$.

In the figures 20 I show the comparision of two similar measurements whereby I use positive driving $\xi_A = 2.5 \times 10^{-5}\,\frac{1}{\mathrm{s}}$ for $t_A = 2000\,\mathrm{s}$ in both cases and after that either $\xi_B = 0\,\frac{1}{\mathrm{s}}$ (example a)or $\xi_B = -1 \times 10^{-5}\,\frac{1}{\mathrm{s}}$ (example b). I show histograms of the droplet volume

density (top), the evolution of the mean radii (mean) and the evolution of the droplet number density for $t > t_A$ (bottom).[11]

In the first 2000 s the driving is still constant, and as before the mean radius is increasing to a value of about $\langle r \rangle \approx 14\,\mu\text{m}$. At a time of $t = 1000\,\text{s}$ there is a rapid increase of droplet volume density which peaks for radii of about 12 to $14\,\mu\text{m}$. The radius of the line of constant volume density (equidensity-line) per radius (yellow) for the characteristic largest droplets is increasing linearly whereby extrapolating this line leads to a value of $5\,\mu\text{m}$ for time 0 s. (Compare this behaviour to 19(d).).
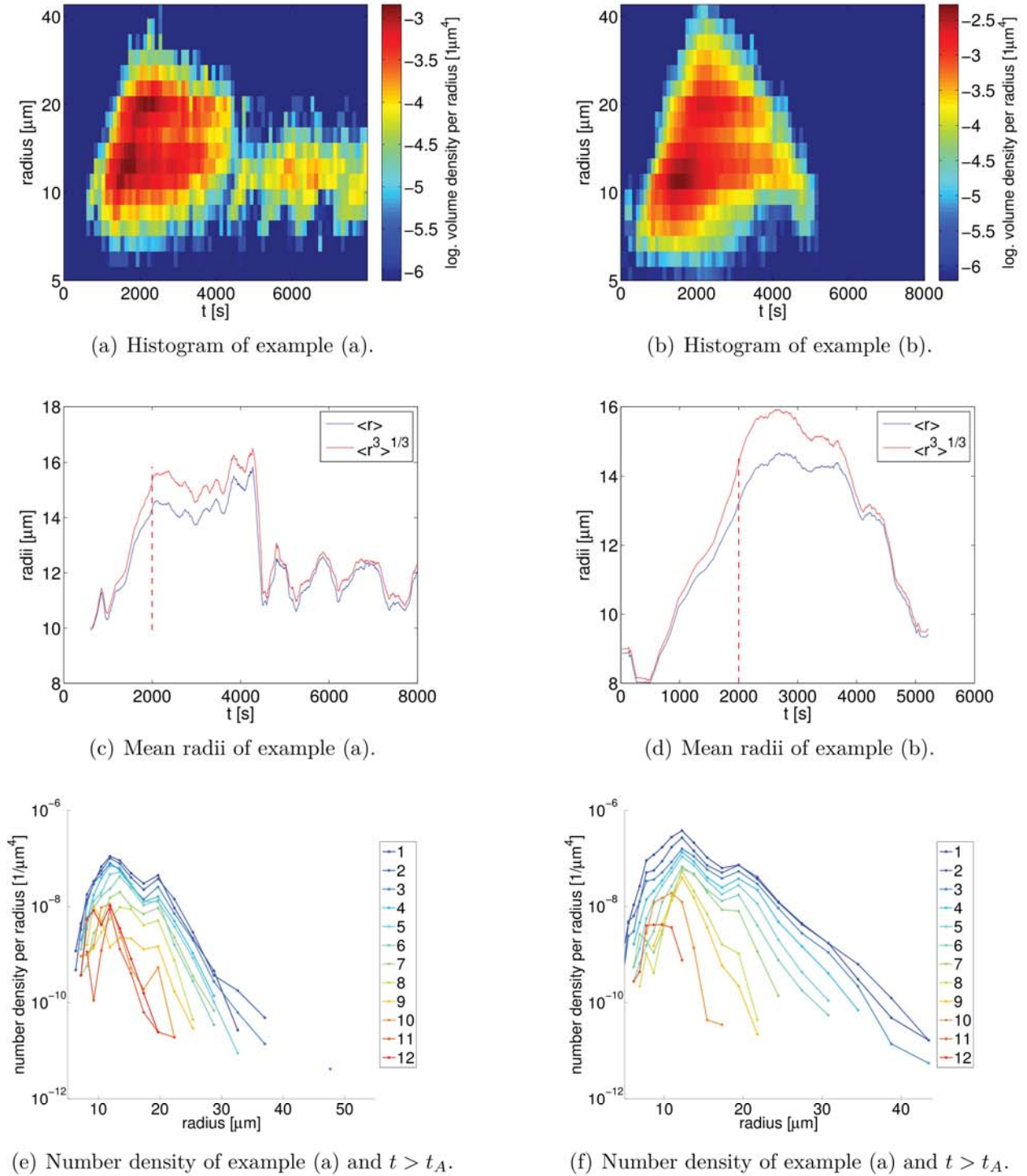
In the succeding 2000 s that equidensity-line is decreasing whereby the mean radius stays constant at about $\langle r \rangle \approx 14\,\mu\text{m}$. In example (b) with negative driving this decrease is nearly linear and much stronger than in example (a).

In example (a) the mean radius is decreasing to about $9\,\mu\text{m}$ within the next 1000 s and at that time the droplet number density deceed 1% of the peak value and after a few hundreds seconds all droplets are vanished. The fact that the driving is negative leads to an evaporations of droplets which explains that behaviour besides the occurring sedimentation.

In example (b) the mean radius is decreasing rapidly to about $12\,\mu\text{m}$ at the time 4000 s and is fluctuating between 11 and $13\,\mu\text{m}$ within the remaining time. The overall droplet number density is fluctuating near the value 8% of the maximal value during this time. A characteristic, fluctuating behaviour can be seen in the histogram 20(a), too.

The period of that variations is in the order of magnitude of about 1000 s which corresponds to the order of magnitude of the period of the convective cell in the bottom layer of the test tube. Because it is plausible that there is a non-constant droplet distribution within the sample I form the hypothesis that regions of characteristic droplet distribution are episodically reaching the observed area due to the convective flow in the cell. Additionally I observe that the period is increasing (see 20(c)) which may occur due to change of the the convection velocity: I expect the velocity to shrink due to a decreasing of the temperature gradients in the system because the temperature variations are dying out due to the constant temperature in the water bath and the flow is slowing down due to viscosity. Actually the amplitude of this effect should decrease due to mixing of the particles within the flow but in figure 20(c) the amplitude is nearly constant over time. One possible expla-

---

[11]It may be noted that the droplet density in case of negative driving ($\xi_B < 0$) is consequently larger by a factor of about 3 although the initial part of the temperature ramp is the same. The peak of the number density is in the order of $3 \times 10^{-6}\,\mu\text{m}^{-3}$ and in the other case in the order of $0.8 \times 10^{-6}\,\mu\text{m}^{-3}$ regardless of similar shape for $t < t_A$. Direct comparision of the acquired raw images show that for $\xi_B < 0$ the illumination is much stronger whereby the droplet size distribution is looking quite similar. I therefore assume that the larger illuminuation leads to an increase of the probability that droplets are illuminated sufficiently strong to be detected. Because the behaviour is similar in both cases I assume that the change of detection probability is independent of the radius. The change in the distribution is limited to an adaption of the normalization constant – its shape is not affected.

(a) Histogram of example (a).

(b) Histogram of example (b).

(c) Mean radii of example (a).

(d) Mean radii of example (b).

(e) Number density of example (a) and $t > t_A$.

(f) Number density of example (a) and $t > t_A$.

Figure 20: *In the figures I compare example (a) in the left figures (a,c,e) and example (b) in the right figures (b,d,f). (a-b) I show two-dimensional histograms of the droplet volume density. (c-d) I show the mean radii $\langle r \rangle$ and $\langle r^3 \rangle^{1/3}$. (e-f) I show the time evolution of the droplet number density per radius bin for the time $t > t_A$. The values are averaged over 300 s.*

nation might be that the sedimentation velocity in fluids is increasing for increasing number densities of particles[8, p. 296]. Because the flow field is near-wall directed downwards and the sedimentation upwards this leads to a focusing of the number densities which may explain the observed effect that there are regularly bunches of droplets with non-decreasing amplitude.[12]

The described behaviour is robust and similarly occurring in about 70 to 80% of the 20 measurements I have done for $\xi_B = 0$.

Indeed I expect that the droplets should vanish after some time due to sedimentation. However, apparently this cannot be seen in the evolution because the measurement ends too early after 8000 s.

I observe in the evolution of the droplet number density for $t > t_A$ in figure 20(e) and 20(f) are remarkable also for another reason: Immeadiately of the jump of ξ, for about 2000 s, the number densities are decreasing with substantially constant shape for all radii. In example (a) the droplets are vanishing after that and in example (b) the distribution is staying substantially constant for $t > 5700$ s after averaging the distributions for 300 s.

3.2.5 Collapse of the droplet size distribution

To analyze the evolution of the droplet number density per radius $n_{\text{th}}(r,t)$ for larger droplets ($r > r_l$) in case of no or small negative driving I assume again that the large droplets sediment towards the meniscus and are thereby growing by collection of smaller droplets. I assume growth by collection is dominant that there is no evaporation in the system such that for both the large droplets and the collected droplets one may safely disregard are shrinking due to diffusion. Furthermore I assume that the considered large droplets will not be collected by even larger droplets.

I assume that the volume growth by collection is proportional to the volume crossed per unit time.

$$\dot{r} = \frac{\kappa}{4} r^2 \varphi_0 \tag{31}$$

when the constant proportional factor, $\varphi_0 > 0$, accounts for the volume fraction of small particles that probably will be collected.

Further I assume that the decrease of droplet number density due to sedimentation is proportional to the ratio of sedimentation velocity $|u_{\text{sed}}| = \kappa r^2$ and a characteristic length scale L which should be of the order of the sample height. I define $n_{\text{th}}(r,t)$ as the droplet number density which derives from this theoretical model whereby $n_r(r,t)$ is the droplet number density per radius in the real system. Neglecting the diffusion term I hence obtain

---

[12]This effect is occurring in a glass of Guinness, too where small bubbles form waves with a characteristic wave length[8, p. 296].

the convection-diffusion equation:

$$\frac{\partial n_{\text{th}}(r,t)}{\partial t} = -\frac{\kappa r^2}{L} n_{\text{th}} - \frac{\partial}{\partial r}\left[\frac{\partial r}{\partial t} n_{\text{th}}\right] \tag{32}$$

$$= -\frac{\kappa r^2}{L} n_{\text{th}} - \frac{\varphi_0}{4}\frac{\partial}{\partial r}\left[\kappa r^2 n_{\text{th}}\right]$$

$$\frac{L}{\kappa r^2}\frac{\partial}{\partial t}\left[\frac{\kappa r^2}{L} n_{\text{th}}\right] = -\frac{\kappa r^2}{L} n_{\text{th}} - \frac{\varphi_0 L}{4}\frac{\partial}{\partial r}\left[\frac{\kappa r^2}{L} n_{\text{th}}\right] \tag{33}$$

Introducing $m(r,t) = \frac{\kappa r^2}{L} n_{\text{th}}$ yields

$$\frac{L}{\kappa r^2}\frac{\partial m(r,t)}{\partial t} = -m(r,t) - \frac{\varphi_0}{4}\frac{\partial m(r,t)}{\partial \frac{r}{L}} \tag{34}$$

and substituting with $\rho := \frac{4r}{\varphi_0 L}$ due to $\varphi_0 > 0$ and $L > 0$ I get

$$\frac{\partial m(\rho,t)}{\partial t} = -\frac{\kappa}{L}\left(\frac{\rho^2 L \varphi_0}{4}\right)^2\left[\frac{\partial m(\rho,t)}{\partial \rho} + m(\rho,t)\right]. \tag{35}$$

Assuming that I can separate $m(\rho,t) = m_\rho(\rho)\, m_t(t)$ I use the ansatz $m(\rho\, t) = \frac{\kappa m_0 n_0}{L}\exp\left[f(\rho) + a\, t\right]$ with the decay constant a and get

$$a = -\frac{\kappa}{L}\left(\frac{L \varphi_0, \rho}{4}\right)^2\left[\frac{\partial f(\rho)}{\partial \rho} + 1\right]. \tag{36}$$

Hence, I obtain

$$f'(\rho) = -\left[1 + \frac{a L}{\kappa}\left(\frac{4}{L \varphi_0 \rho}\right)^2\right]$$

$$\Rightarrow f(\rho) = -\rho + \frac{a L}{\kappa \rho}\left(\frac{4}{L \varphi_0}\right)^2 \tag{37}$$

and therefore

$$m(\rho,t) = \frac{\kappa m_0 n_0}{L}\exp\left[-\rho + \frac{a L}{\kappa \rho}\left(\frac{4}{L \varphi_0}\right)^2 + a\, t\right]$$

$$\Rightarrow n_{\text{th}} = \frac{n_0 m_0}{r^2}\exp\left[-\frac{4}{\varphi_0 L} r + \frac{4a}{\varphi_0 \kappa}\frac{1}{r} + a\, t\right]. \tag{38}$$

By inspection one readily verifies that this function solves equation (33).

The overall droplet number density of the detected droplets is given by $n(t) = \int_0^\infty n_{\text{th}} dr$.

Using equation (38) I obtain

$$
\begin{aligned}
\frac{\mathrm{d}n(t)}{\mathrm{d}t} &= \frac{\mathrm{d}}{\mathrm{d}t} \int_{r_{\min}}^{r_{\max}} n_{\text{th}} \mathrm{d}r \\
&= \int_{r_{\min}}^{r_{\max}} \frac{\partial n_{\text{th}}}{\partial t} \mathrm{d}r \\
&= e^{at} \int_{r_{\min}}^{r_{\max}} \frac{m_0\, L}{\kappa\, r^2} \exp\left[-\frac{4}{\varphi_0\, L} r + \frac{4a}{\varphi_0\, \kappa} \frac{1}{r} \right] \mathrm{d}r \\
&= C e^{at} \\
\Rightarrow n(t) &= n_0 e^{at}.
\end{aligned}
\tag{39}
$$

where $n_0 = n(t=0)$ and $c = a\, n_0$.

Therefore I get

$$
\frac{r^2\, n_{\text{th}}}{n(t)} = m_0 \exp\left[-\frac{4r}{\varphi_0\, L} + \frac{4a}{\varphi_0\, \kappa} \frac{1}{r} \right]
$$

$$
\log\left(\frac{r^2\, n_{\text{th}}}{n(t)} \right) = \log m_c + \left[-\frac{4r}{\varphi_0\, L} + \frac{4a}{\varphi_0\, \kappa} \frac{1}{r} \right].
\tag{40}
$$

Plotting $\log\left(\frac{r^2\, n_r(r,t)}{n(t)} \right)$ as function of r should therefore yield a collapse of all distributions for all times. After all the right hand side of equation (40) is independent of the time and depends only on r and the constants φ_0, a and L.

In figure 21 I show the resulting plot of example (a) and (b).

(a) Collapse in example (a).

(b) Collapse in example (b).
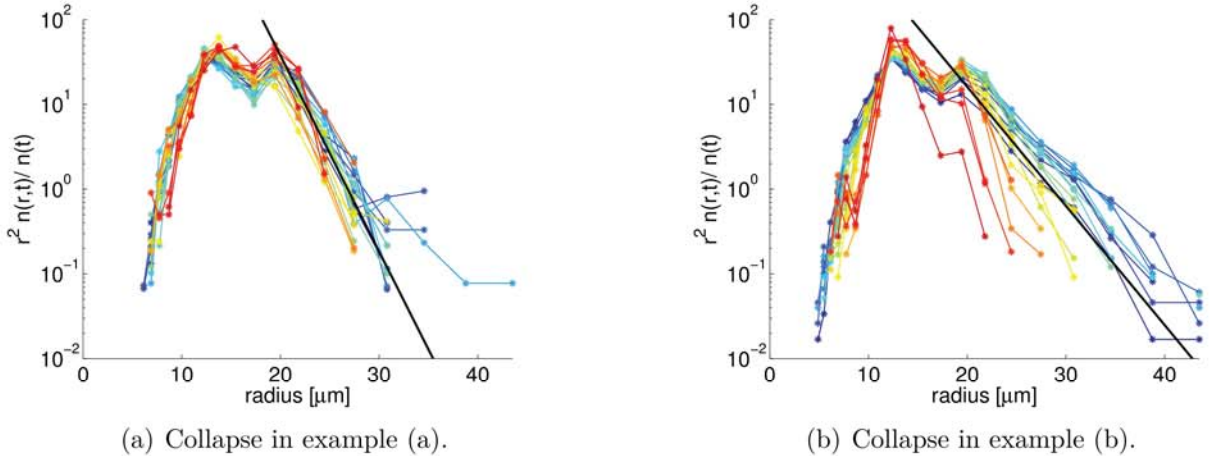
Figure 21: *Collapse of the droplet size distribution for the first* 2000 s *after the of the driving for example (a) and (b). I also show a linear fit for larger radii described in section 3.2.6.*

I see that in principle the curves a collapsing at least for parts of the time in those two expamples. In it seems sufficient for the time of 2000 s and for all radii smaller than 30 μm.

In the collapse seems to be sufficient at least for a time of 1200 s and for all radii. This collapse time is in the order of magnitude of the time of single precipitation events which as about 2000 s (see section 3.2.3).

3.2.6 Scales of the system

Equation (40) has three free parameters which will be determined as follows:

To obtain the decay constant a I plot the overall droplet number density $\log[n(t)]$ in dependence of the time t and compute the slope m_n. Due to equation (39) we know

$$a = m_n. \tag{41}$$

In figure 22 I show the progression of $n(t)$ for 2000 s after t_A in the two exemplary measurements (a) and (b) where $n(t)$ is calculated for the corresponding time bins. Equation (39) provides a good description of $n(t)$ for a time of an order of magnitude of 1000 to 2000 s in that example. The decay constant yields about $-1.0 \times 10^{-3}\,\frac{1}{\mathrm{s}}$ in example (a) and $-1.3 \times 10^{-3}\,\frac{1}{\mathrm{s}}$ in example (b).

(a) $n(t)$ in example (a).   (b) $n(t)$ in example (b).
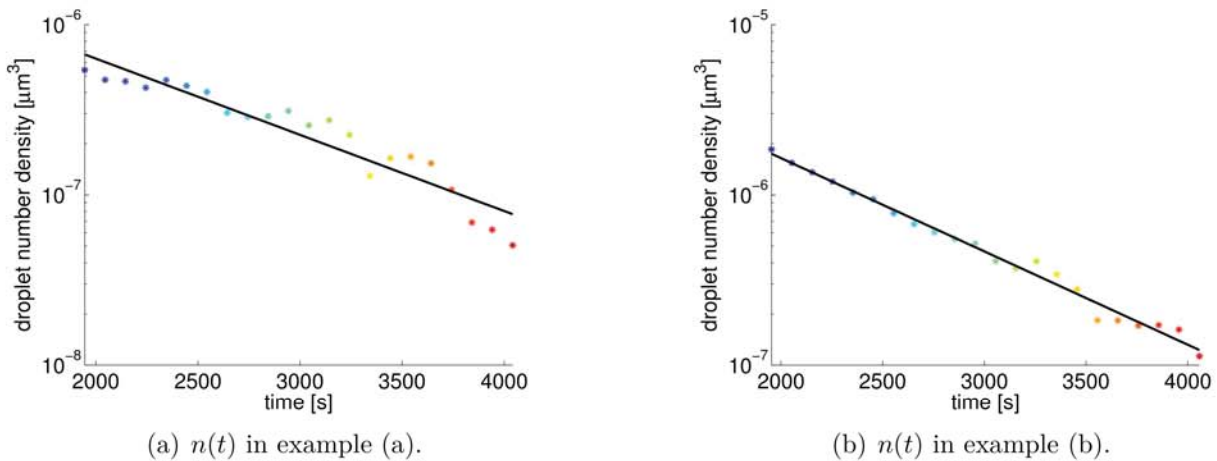
Figure 22: *The fit fo the exponential decay of the overall droplet number density fit for a time interval of 2000 s after the jump of the driving in example (a) and (b).*

To calculate the length scale L, I start from equation (40) and calculate the radius r_c at

the maximum of the right side via

$$
\begin{aligned}
0 &= \frac{\mathrm{d}}{\mathrm{d}r}\left[-\frac{4r_c}{\varphi_0\,L} + \frac{4a}{\varphi_0\,\kappa}\frac{1}{r_c}\right] \\
&= -\frac{4}{\varphi_0\,L} - \frac{4a}{\varphi_0\,\kappa}\frac{1}{r_c^2} \\
\Rightarrow r_c &= \left(\sqrt{\frac{\kappa}{L\,a}}\right)^{-1}
\end{aligned}
\tag{42}
$$

yielding

$$
L = -\frac{\kappa\,r_c^2}{a} = -\frac{\kappa\,r_c^2}{m_n}.
\tag{43}
$$

In the collapsed graphes 21 I examine the value r_c where the normalized distribution $\frac{n_r(r,t)\,r^2}{n(t)}$ has the maximal value. Firstly I observe that there is a local minima for about $18\,\mu m$ which I cannot explain using the equation. Because the derivation of L is considering the maximum of $\frac{n_{\mathrm{th}}\,r^2}{n(t)}$ which has no local minima there I estimate the maxima by extrapolating the two branches of the remaing, collapsed data. I obtain $r_c = 17(3)\,\mu m$ in example (a) $r_c = 16(3)\,\mu m$ in example (b) and thereby length scales $L = 1.2(4)\,cm$ (example a) and $L = 0.8(3)\,cm$. The uncertainty of r_c is dominating the error in L such that the error of κ and m_n need not be addressed here.

Those values are in the order of magnitude of the height of the bottom layer in the sample which seems justified.

To obtain the collection constant φ_0 I use the asymptotic slope for large radii in equation (40),

$$
\begin{aligned}
m_{r>r_l} &= -\frac{4}{\varphi_0\,L} \\
\Rightarrow \varphi_0 &= -\frac{4}{m_{r>r_l}\,L}.
\end{aligned}
\tag{44}
$$

To get a valid estimate of the slope I have to restrict the regime of the used time and radius bins. To this end I check for how long the curves agree with the asymptotic regime. In example (a) I use $t_A = 2000\,s < t < 4000\,s$ and $20\,\mu m < r < 40\,\mu m$ and in example (b) $t_A < t < 3500\,s$ and $20\,\mu m < r < 32\,\mu m$. This yields to collection constants of $\varphi_0 = (7\pm3)\cdot10^{-4}$ in example (a) and $(20\pm7)\cdot10^{-4}$ in example (b) whereby the error is estimated by propagating the error of L.

This values seem to be in a justified order of magnitude because the overall droplet volume density lies in the regime of 1 to 3% in the maximum and we expect that only a fraction of the droplets will be collected by larger droplets.

In figure 3.2.5 with negative driving (example b) I see that the branch of the collapsed

graph for larger radii is shifting towards smaller radii. Because the shrinking of droplets with a radius in the regime of 20 to $40\,\mu$m due to the negative driving of $\xi_B = -1 \times 10^{-5}\,\frac{1}{\text{s}}$ is not dominant the shifting may be explained due to a reduction of φ_0 which may occur through diffusion of the smaller droplets which are collected and by the collection of those droplets during the sedimentation.

4 Conclusion

4.1 Summary

In section 2 I observe synchronization of episodic precipitation in a binary fluid and square-wave external driving if we numerically integrate the model described in section 1.4. I show that this model leads to Arnold tongues for period-n-cycles for $n \in [1,2,3]$ where the with of the period-1 Arnold tongues increases linearly for increasing amplitude of the external driving. Besides smaller differences the phase of the stable fixed point within the computed period-1 Arnold tongues shows an universal behaviour: The phase is increasing nearly linearly from 0 at the left border to 0.5 at the right border of the tongues independently of the amplitude and the tongue. Regarding the size of the synchronization regime and the phase of the stable fixed points my results are in contrast to experimental work done by Julian Vogel in [22] who observed synchronization even for parameters which are far beyond my Arnold tongues and phases which are systematically shifted.

In section 3 I reproduced episodic precipitation experimentally and examined the characteristic behaviour of the evolution of droplet size distribution for positive and constant driving as described by Martin Rohloff in [20].

Subsequently, I examined the evolution of droplet size distribution for negative and zero driving and used a model to collapse the size distributions successfully on each other for a time scale of the order of magnitude of single precipitation events. This model neglects diffusion and assumes that the considered large droplets are sedimenting length scale and thereby are collecting droplets with a constant volume density of collected droplets. I hereby get another parameter which describes the decay of the overall droplet number density which I can fit using the data but its meaning and dependencies from other parameters that so far have been completely unknown.

Using two exemplary measurements I obtain sedimentation length scales of about 1 cm, which corresponds to the height of the considered layer of my test tube, and I get values for the volume density of collected droplets of the order of magnitude of 10^{-3} which is about one order smaller than the measured ovall volume density.

4.2 Outlook

The discrepancy in my numerical results on synchronization and Julian VOogel's experimental results calls for further studing to facilitate deeper insights into the droplet growth and episodic precipitation in binary fluids. In particular I suggest to examine the Arnold tongues occurring in the experimental model system which would turn out to be effortful

due to the necessary scanning of the parameter space. In particular it would be of interest to check whether Julian's observations of frequency locking even in cases which lie far outside the computed Arnold tongues are reproducable and whether one can observe Arnold tongues of higher order at all. Within that scope it would be worthwile to study the phase of nucleation in the period-1 Arnold tongues to examine whether we observe a characteristic universal behaviour comparable to my numerical results. In particular one could use the experimental method used in the second part of the present thesis to examine whether the phase of nucleation is systematically in the regime of larger driving.

For further analysis of the evolution of the droplet size distribution I want to understand the considered decay constant and whether and how it depends on the sedimentation velocities. To address this problem we need measurements different temperatures and correspondingly different velocities. In addition it would be interesting to study the behaviour of the volume density of the collected droplets in dependence of the sedimentation time and the rate of diffusion. I have done about 50 further measurements which I could use to analyze whether the observed effects and values for the length scale and volume density of collected droplets is robust and to investigate the parameters.

In contrast to the model described in section 2 this model depends on the size distribution and not only on a characteristic droplet size. This motivates me to further investigation of that new approach depending on the distribution and several parameters.

A Appendix

Material Constants of Iso-Butoxyethanol and Water

This chapter is a copy from the Bachelor thesis of Julian Vogel [22] where he reproduced the data for material constants. Those data have been collected and measured by T. Lapp et. al. [12].

The index $i \in \{IBE,W\}$ will be used to refer to material properties of IBE and water, respectively, and in accordance with the phase diagram 3(a) the concentration are always given in terms of $\phi = \phi_{IBE}$.

Density (based on [7])

The densities of the phases are determined by the composition, thermal expansion and molar excess volume,

$$\rho(\phi^m, T) = \left[\frac{\phi^m}{\rho_{IBE}} + \frac{(1 - \phi^m)}{\rho_W} + \left(\frac{\phi^m}{M_{IBE}} + \frac{(1 - \phi^m)}{M_W} \right) V_E^n \right]^{-1}. \tag{45}$$

where $\rho_i = \rho_i(T)$ are the (temperature-dependent) densities of the pure substances, M_i their molar masses, and $V_E^n = V_E^n(\phi^n)$ is the molar excess volume.

The molar masses, M_i are 18.01528 g/mol for water[16] and 118.17416 g/mol for IBE[17], respectively.

The temperature dependence of the density, $\rho_i(T)$, of the pure substances is linearly approximated around $T_0 = 25°C$,

$$\rho_i(T) = \rho_i(T_0) - \alpha_i \cdot (T - T_0) \tag{46}$$

with fit parameters for ρ_i and α_i given in table 1.

	$\rho_i(T_0)$ [g cm^{-3}]	α_i [g cm^{-3} K^{-1}]
water	0.997043	0.2571×10^{-3}
IBE	0.886255	0.968×10^{-3}

Table 1: *Densities and thermal expansion coefficients for water and IBE [according to 7]*

Moreover, the molar excess volume is fitted like [7]:

$$V_{\mathrm{E}}^n(\phi^n) = \frac{\phi^n\,(1-\phi^n)}{1 - G\,\tilde{\phi}} \cdot \left(A_1 + A_2\,\tilde{\phi} + A_3\,\tilde{\phi}^2\right) \tag{47}$$

$$\text{with} \quad \tilde{\phi} = 1 - 2\phi^n$$

$$\text{and} \quad G = 0.975\,,$$

$$A_1 = -3.079 \ \mathrm{cm^3/mol}\,,$$

$$A_2 = 1.801 \ \mathrm{cm^3/mol}\,,$$

$$A_3 = 0.839 \ \mathrm{cm^3/mol}\,.$$

A slight temperature dependence of these fit parameters was reported by [7]. However, it is so small that we need not take it into account here.

To get the dependence of the density difference on the reduced temperature the dependence $\phi(\theta)$ (coexistance curve) has to be inserted into equation 45.

Viscosity (own measurements augmented by data of [25] and [14])

We first provide the data of the pure phases, and then obtain the viscosity of the mixture by appropriate interpolation.

The viscosity of IBE was measured with an Ubbelohde viscosimeter type 537 10/I made by Schott. The temperature dependence of the viscosity η is fitted by

$$\eta_i(T) = A_i \times 10^{\frac{B_i \cdot (T_0 - T) - C_i \cdot (T_0 - T)^2}{T + D_i}} \tag{48}$$

with $T_0 = 20°$ C and coefficients given in table 2. The values for water are taken from [25].

	A [kg m^{-1} s^{-1}]	B	C [(° C)$^{-1}$]	D [° C]
water	1.002×10^{-3}	1.3272	0.001053	105
IBE	3.36×10^{-3}	1.730	0.001	108

Table 2: *Fit coefficients for the viscosity of water and IBE, defined by equation (48), the data is taken from [25]*

To interpolate the viscosities for a mixed phase of given mass fraction ϕ^m we use the composition-dependent viscosities at 25°C for a homogeneous mixture in the single-phase regime, as provided by [14]. The data is fitted with a fifth order polynomial

$$\eta(\phi^m, T = 25°\mathrm{C}) = -40.66\,(\phi^m)^5 + 103.44\,(\phi^m)^4 - 100.32\,(\phi^m)^3$$
$$+ 39.35\,(\phi^m)^2 + 0.17\,\phi^m + 0.91. \tag{49}$$

Assuming that the coefficients of interpolation are not changing substantially in the temperature range of our measurements, a rescaled viscosity $\tilde{\eta}(\phi^m)$ is defined. It only depends on

the composition ϕ^m

$$\eta(\phi^m, T) = \tilde{\eta}(\phi^m) \cdot \eta_{\mathrm{IBE}}(T) + [1 - \tilde{\eta}(\phi^m)] \cdot \eta_{\mathrm{W}}(T) . \tag{50}$$

To check the strong assumption entering this interpolation, we also measured the viscosity of the two phases at $T = 40°\mathrm{C}$. For both phases the prediction of (50) was accurate to within 2%. This is sufficient for our means.

References

[1] Günter K Auernhammer, Doris Vollmer, and Jürgen Vollmer. "Oscillatory instabilities in phase separation of binary mixtures: Fixing the thermodynamic driving". In: *The Journal of Chemical Physics* 123.13 (2005), p. 134511.

[2] George Keith Batchelor. *An introduction to fluid dynamics*. Cambridge University Press, 2005.

[3] David Bolton. "The computation of equivalent potential temperature". In: *Monthly Weather Review* 108.7 (1980), pp. 1046–1053.

[4] AJ Bray. "Theory of phase-ordering kinetics". In: *Advances in Physics* 43.3 (1994), pp. 357–459.

[5] Michael D Clark et al. "Focusing nanocrystal size distributions via production control". In: *Nano Letters* 11.5 (2011), pp. 1976–1980.

[6] Robert L Devaney, Luke Devaney, and Luke Devaney. *An introduction to chaotic dynamical systems*. Vol. 6. Addison-Wesley Reading, 1989.

[7] Hideshige Doi, Katsutoshi Tamura, and Sachio Murakami. "Thermodynamic properties of aqueous solution of 2-isobutoxyethanol at T=(293.15, 298.15, and 303.15) K, below and above LCST". In: *The Journal of Chemical Thermodynamics* 32.6 (2000), pp. 729–741.

[8] Andrew Cadle Fowler. *Mathematical models in the applied sciences*. Vol. 17. Cambridge University Press, 1997.

[9] Ernst Hairer, Syvert Paul Nørsett, and Gerhard Wanner. *Solving ordinary differential equations I: nonstiff problems*. Vol. 1. Springer Science & Business, 2008.

[10] Robert A Houze. *Cloud Dynamics, vol. 53 of the International Geophysics Series*. 1993, 1st edition.

[11] Tobias Lapp. "Evolution of Droplet Distributions in Hydrodynamic Systems". PhD thesis. Niedersächsische Staats-und Universitätsbibliothek Göttingen, 2012.

[12] Tobias Lapp, Martin Rohloff, and Jürgen Vollmer. "Episodic Precipitation". unpublished. 2014.

[13] Tobias Lapp et al. "Particle tracking for polydisperse sedimenting droplets in phase separation". In: *Experiments in fluids* 52.5 (2012), pp. 1187–1200.

[14] K. Menzel, S. Z. Mirzaev, and U. Kaatze. "Crossover behavior in micellar solutions with lower critical demixing point: Broadband ultrasonic spectrometry of the isobutoxyethanol-water system". In: *Phys. Rev. E* 68 (2003), p. 011501.

[15] Arkady Pikovsky, Michael Rosenblum, and Jürgen Kurths. *Synchronization: a universal concept in nonlinear sciences*. Vol. 12. Cambridge University Press, 2003.

[16] National Center for Biotechnology Information PubChem. *PubChem Compound Database*. CID=962 (17 July 2013). National Center for Biotechnology Information. 2013. URL: http://pubchem.ncbi.nlm.nih.gov/summary/summary.cgi?cid=962.

[17] National Center for Biotechnology Information PubChem. *PubChem Compound Database*. CID=521158 (17 July 2013). National Center for Biotechnology Information. 2013. URL: http://pubchem.ncbi.nlm.nih.gov/summary/summary.cgi?cid=521158.

[18] Gerard H Roe. "Orographic precipitation". In: *Annual Review Earth Planetary Sciences* 33 (2005), pp. 645–671.

[19] Walter Roedel and Thomas Wagner. *Physik unserer Umwelt: Die Atmosphäre*. Vol. 1. Springer, 1992.

[20] Martin Rohloff. "Measuring the droplet-size and velocity distributions in binary phase separation." Diploma Thesis. Georg-August-Universität Göttingen, 2011.

[21] F.W. Taylor. *Elementary Climate Physics*. Oxford University Press, 2005.

[22] Julian Vogel. "The Influence of Stirring and Time-Dependent Driving on the Formation of Precipitation". Bachelor Thesis. Georg-August-Universität Göttingen, 2013.

[23] Jürgen Vollmer, Ariane Papke, and Martin Rohloff. "Ripening and focusing of aggregate size distributions with overall volume growth". In: *Frontiers in Physics* 2.18 (2014).

[24] Lian-Ping Wang and Wojciech W Grabowski. "The role of air turbulence in warm rain initiation". In: *Atmospheric Science Letters* 10.1 (2009), pp. 1–8.

[25] R. C. Weast. *CRC Handbook of Chemistry and Physics*. Ed. by R. C. Weast, M. J. Astle, and W. H. Beyer. 69. CRC Press, Inc. Boca Raton, Florida, 1988-1989.

[26] Julia M Yeomans. *Statistical mechanics of phase transitions*. Oxford University Press, 1992.

List of Figures

Acknowledgements

My thesis is directly based on prior work of Jürgen Vollmer, Tobias Lapp, Martin Rohloff and Julian Vogel and is standing on the shoulders of giants. I therefore want to thank them and – of course – the whole science community to make this thesis possible.

I am very grateful to my supervisors Jürgen Vollmer and his doctoral student Martin Rohloff.

Jürgen gave me many and deep insights in the physics of binary fluids and the methodology of scientific research. He provided helpful advices throughout my thesis and discussed occurring problems even late after midnight. Special thanks go to him because he is on of the few who has hours of labor which have a significant overlap with mine.

Martin supervised my work in the laboratory, answered my questions concerning his *Matlab* scripts. I benefitted from his ideas and his advice, too.

Additionally I am grateful for numerous advices throughout my project given by Artur Wachtel, Johannes Blaschke, Jakob de Mayer, Bernhard Altaner, Laura Stricker et al.

I want to thank Sonka Reimers to declare herself spontaneously ready to deliver my thesis to the examination office due to my non-attendance.

Lately I would like to thank the whole working group of Jürgen Vollmer and Marco Mazza for their good company and the enjoyable working atmosphere. In particular I appreciated many discussions with them concerning physics and other topics and spending free time together.